nature biomedical engineering

Article

A temperature-responsive intravenous needle that irreversibly softens on insertion

Karen-Christian Agno[1,5], Keungmo Yang[2,3,5], Sang-Hyuk Byun [1], Subin Oh [1], Simok Lee[1], Heesoo Kim[1], Kyurae Kim [2], Sungwoo Cho[1], Won-Il Jeong [2] ✉ & Jae-Woong Jeong [1,4] ✉

The high stiffness of intravenous needles can cause tissue injury and increase the risk of transmission of blood-borne pathogens through accidental needlesticks. Here we describe the development and performance of an intravenous needle whose stiffness and shape depend on body temperature. The needle is sufficiently stiff for insertion into soft tissue yet becomes irreversibly flexible after insertion, adapting to the shape of the blood vessel and reducing the risk of needlestick injury on removal, as we show in vein phantoms and ex vivo porcine tissue. In mice, the needles had similar fluid-delivery performance and caused substantially less inflammation than commercial devices for intravenous access of similar size. We also show that an intravenous needle integrated with a thin-film temperature sensor can monitor core body temperature in mice and detect fluid leakage in porcine tissue ex vivo. Temperature-responsive intravenous needles may improve patient care.

Intravenous (IV) injection is one of the commonly used interventions in healthcare settings worldwide[1–6], with approximately 150 million IV devices used annually in the United States[7]. IV injection is primarily used in situations that require faster delivery of therapeutic drugs[8], when oral medication is not feasible, or when the medication will result in irritation once injected into skin or muscle[9]. The common IV procedure in a healthcare facility involves insertion of a needle into the patient's peripheral vein, and a complete IV infusion usually takes from a few hours to a couple of days[8,10], depending on the physician's assessment of the patient's condition. Depending on the type of IV access device used, an IV procedure can either have an outer thin polymeric tube (over-the-needle catheter) or a shorter needle with a winged end, which is carefully advanced and lodged inside the vein[11].

Although these IV needles are easy to place, their rigid structure, which does not mechanically match the biological tissue, can cause critical problems for both patients and healthcare providers. Tissue damage, particularly at the patient's injection site, which is often associated with the average dwell time of a catheter[8,10,12], is inevitable. The difference in mechanical properties between commercial IV access devices and soft tissue can rupture the thin-walled vein during dynamic movement at the IV site (that is, forearm, back of the hand and antecubital fossa) and cause inflammation, obstruction and fluid leakage[8,10,13–16]. This not only restricts the patient's motion and necessitates replacement or re-siting of rigid IV catheters every 72–96 hours, which is a discomfort to hospitalized patients[17] but it can also lead to prolonged hospitalization, delayed treatment and increased morbidity[18,19].

Several approaches to help alleviate tissue damage involving IV access devices generally explore the modification of the needle–catheter geometric structure (for example, by shortening the catheter length[12], by varying the catheter tip structure[20] or via a hydrogel coating the needle[21]) and the reformulation of the catheter's polymeric material for enhanced biocompatibility and antibacterial properties[22]. Despite the improvements achieved so far, the existing materials used in manufacturing IV access devices have high and fixed stiffness

[1]School of Electrical Engineering, Korea Advanced Institute of Science and Technology (KAIST), Daejeon, Republic of Korea. [2]Graduate School of Medical Science and Engineering, Korea Advanced Institute of Science and Technology (KAIST), Daejeon, Republic of Korea. [3]Division of Gastroenterology and Hepatology, Department of Internal Medicine, College of Medicine, The Catholic University of Korea, Seoul, Republic of Korea. [4]KAIST Institute for Health Science and Technology, Daejeon, Republic of Korea. [5]These authors contributed equally: Karen-Christian Agno, Keungmo Yang. ✉e-mail: wijeong@kaist.ac.kr; jjeong1@kaist.ac.kr

(at least tens to hundreds of megapascals[23–25], which is four to seven orders of magnitude higher than the stiffness of biological tissue[26]). Tissue–cannula modulus mismatch causes tissue trauma that may only become apparent several hours to days after IV placement[12], and may last up to several days even after the infusion is complete[16]. Furthermore, healthcare providers who handle sharp medical devices are at high risk of needle-related incidents, particularly after needle use[27]. Needle-related incidents are commonly associated with a high exposure risk to blood-borne pathogens, particularly human immunodeficiency virus (HIV) and hepatitis B and C virus (that is, HBV and HCV, respectively), with IV needles being associated with the greatest risk of transmitting these viruses because of their direct contact with blood[28]. Blood-borne pathogen transmission is detrimental to human health, and such transmission has been reported to be most prevalent among healthcare providers due to accidental needlestick injuries after needle use[29]. Since the World Health Organization (WHO) called for the use of smart syringes in 2015, safety-engineered syringes and needles (that is, a syringe or needle with a built-in safety mechanism to reduce the risk of needlestick injuries to healthcare workers) have been developed and are commercially available[30,31]. Although these devices were reported to decrease a number of percutaneous injuries[32], the needle remains rigid after use and has the potential risk of inducing accidental needlestick injury[30].

Here we present the design and operation of a phase-convertible, adapting and non-reusable (P-CARE) needle that facilitates needle stiffness-tuning for an enhanced tissue–needle compatibility and after-use safety-handling mechanism. The P-CARE needle is functionalized by gallium (melting temperature (T_{melt}) = 29.76 °C), which forms a hollow rectangular needle structure encapsulated with a high-tear-strength, soft polymer. The needle has an adaptable, stand-alone modulus control capability, thereby providing high stiffness for rigid insertion into soft tissues at room temperature (below 30 °C) and tissue-like softness once inside the tissue bed (~37 °C), with continuous fluid delivery even during tight bending. After use, the needle remains completely soft, preventing unethical reuse of the needle and needlestick injuries. To further enhance patient care, we integrated a thin-film temperature sensor with the P-CARE needle to monitor the core body temperature or unintended leakage of infused fluid in the subcutaneous layers, eliminating the need for additional medical tools or procedures.

We performed a series of studies that provide a fundamental understanding of the thermal, mechanical and electrical characteristics of the P-CARE needle with in-body temperature sensing and verify its potential utility for IV administration. In addition, in vivo experiments in mice show that this softening needle can notably reduce tissue injury at an injected site compared with commercial rigid IV access devices of comparable size because of the ability of the P-CARE needle to highly conform to dynamic deformation of soft tissue during motion. Additional proof-of-concept demonstrations in both in vivo and porcine tissue confirm the capability of the P-CARE needle embedded with a thin-film sensor to monitor the on-site temperature, highlighting its potential use for sensing the core body temperature or unintended drug leakage within tissue. Overall the P-CARE needle addresses not only the WHO's call for the development of smart needles for one-time use but also fosters patient care with its enhanced tissue–needle mechanical compatibility and capability to monitor a vital sign (that is, body temperature) or drug delivery at the injected site with no additional medical equipment or procedure.

Results

Design, material and operation of the P-CARE needle

Figure 1a shows a diagram of the P-CARE needle. The various components of the needle can be grouped into two parts: (1) the rectangular needle frames (grey, for needle stiffness), and (2) the soft polymeric encapsulations (red, for the needle sheath). The needle frames are made from gallium shaped into two U-channel structures (outer height (h) × width (w) × length (l), 0.90 mm × 1.05 mm × 25 mm; inner $h × w × l$, 0.70 mm × 0.85 mm × 25 mm; the upper and the side wall thickness for each frame is 0.20 mm and 0.10 mm, respectively). The outer U-channel frame is placed over the inner U-channel platform, enclosing both its side walls to form a closed, rectangular hollow architecture and is then encapsulated using silicone with excellent tear strength (Elastosil RT 623, >30 N mm⁻¹; thickness of 0.15 mm for the outer sheath and 0.10 mm for the inner sheath). Gallium is an optimal material for developing medical needles with variable stiffness due to its phase convertibility between solid (elastic modulus of 9.8 GPa) and liquid[33,34], low T_{melt} (29.76 °C)[35] and biocompatibility[35–37]. The completed needle has outer dimensions of 1.20 mm (h) × 1.35 mm (w) and inner channel dimensions of 0.30 mm (h) × 0.45 mm (w), which are comparable to the commercial 18 G IV catheter (outer diameter), 1.3 mm). Supplementary Fig. 1 shows the step-by-step fabrication process for the P-CARE needle. In line with this, the dimensions of the gallium-based needle could be reduced further by using thermal drawing, which is a commonly used strategy in creating optical fibre[38–40]. Another possible method involves integrating a polymer-based stiffening channel using gallium and microfluidic channel by stacking[41], a method usually used in deformable, soft neural probes. However, it should be noted that further downscaling the gallium-based needle has a trade-off between its mechanical properties and insertion performance. To add more functionality and improve patient welfare, a thin-film temperature sensor (inset in Fig. 1a) can be embedded with the needle to monitor on-site temperature. The design and operation details of the temperature sensor are given in Supplementary Fig. 2. The stiffness and shape of the P-CARE needle can be tuned as shown in Fig. 1b. The needle is rigid and straight at room temperature, like the conventional medical needle, but becomes soft and compliant when a temperature of ~30 °C or above is applied because of the liquefaction of the encapsulated gallium frame. Figure 1c shows this stiffness-tuning characteristic along with the ability to reliably deliver fluid even in a soft, highly deformed state.

The key features of the P-CARE needle for healthcare IV use are illustrated in Fig. 1d. In rigid mode, the needle can puncture the soft biological tissue. The needle then becomes soft due to the local tissue temperature and can dynamically adapt to tissue deformation while reliably delivering fluid. The same IV needle after use is completely soft, making it entirely non-reusable. These advancements on IV needles not only enhance patient care for IV administration but also reduce potential risk of transmitting deadly blood-borne pathogens (such as HIV, HBV and HCV) among patients and healthcare workers through accidental needle injuries and unethical reuse of needles. Figure 1e shows the comparison of the P-CARE needle with existing commercial IV access devices that are commonly used in hospital settings (IV metal needle is stainless steel, with a modulus of ~200 GPa; IV catheter is fluorinated ethylene propylene, with a modulus of ~400 MPa (ref. 25)). To determine the stiffness-varying and tissue-adapting capability of the P-CARE needle, we used transparent, soft-tissue phantoms (modulus of 415 kPa, mimicking the property of veins[42]; 10% oil in 33:1 polydimethylsiloxane (PDMS)) with an ~5-mm-diameter vein structure that served as the insertion medium (Fig. 1f). We showed that the rigid P-CARE needle can penetrate the soft synthetic tissue similarly to commercial IV access devices at ambient room temperature (Fig. 1f, top) and that the needle softens as it stays inside the soft-tissue phantom (~37 °C; Fig. 1f, bottom). In addition, the softened needle conformally adapts to the deformation of tissue without risk of damaging the vein, which cannot be done by the commercial IV stainless-steel needle and catheter. Stiffness-tuning with superior tissue adaptability is a unique feature of the P-CARE needle that overcomes the fundamental limitation of the conventional IV access devices, which have intrinsically high and fixed stiffness and can lead to tissue trauma at the injection site, particularly when the patient moves, because of the large mechanical mismatch between the rigid needle and soft tissue[34,43–45].
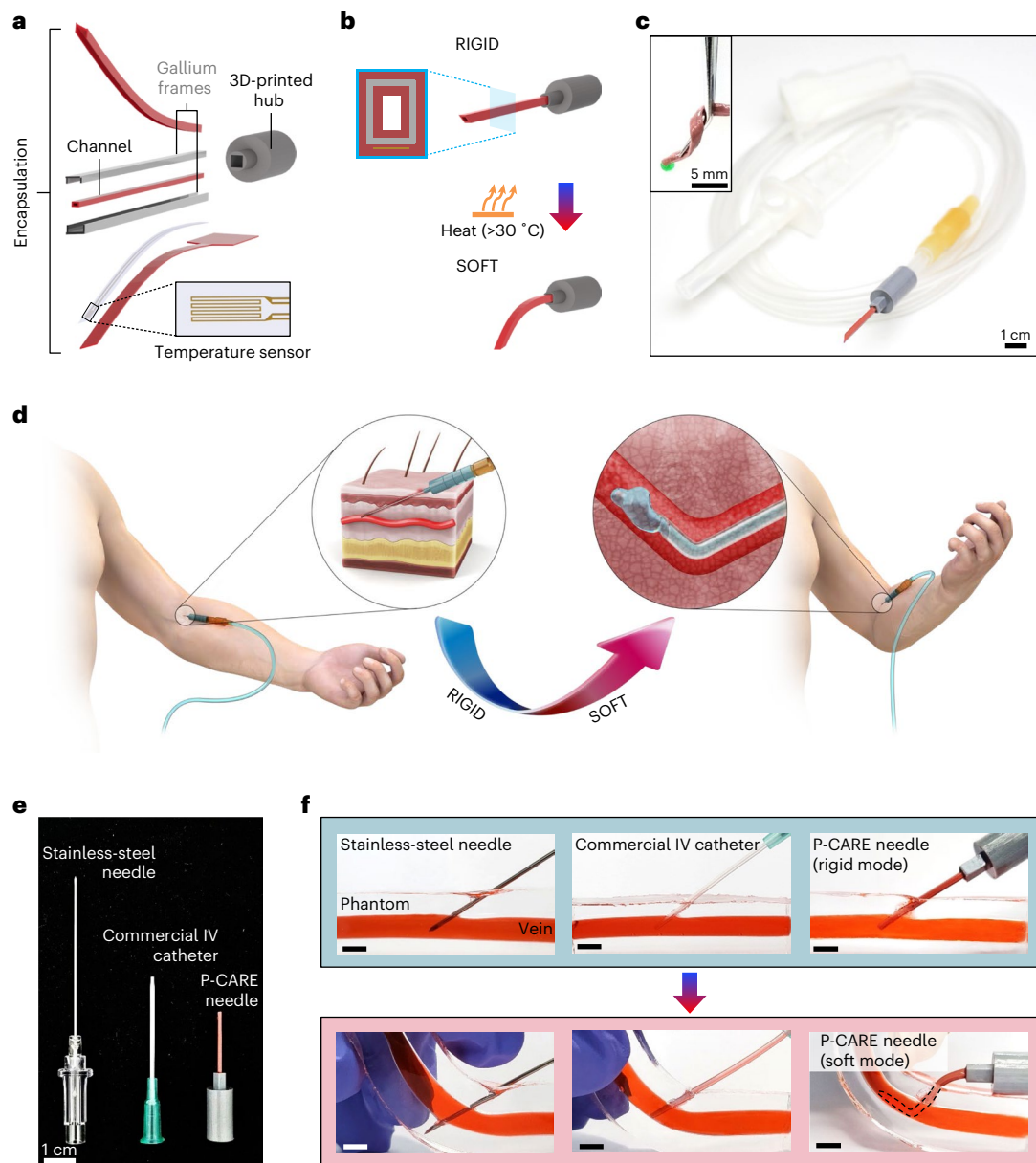
Fig. 1 | Design and operating principles of a P-CARE needle. a, Enlarged view of a P-CARE needle, consisting of a rectangular hollow needle structure made with gallium (T_{melt} = 29.76 °C), a thin-film temperature sensor, soft polymeric channel and encapsulations, and a 3D-printed needle hub. The inset shows the magnified view of the temperature sensor. **b**, Conceptual illustration of the needle stiffness control with temperature. The inset shows the cross-section of the P-CARE needle. **c**, Photograph of a P-CARE needle in rigid mode for IV medication. Inset: the same needle in soft mode, showing high deformability with reliable fluid delivery. **d**, Conceptual illustration of the key features of the P-CARE needle. At room temperature the needle is rigid and straight, allowing facile tissue penetration, much like conventional IV needles (left inset: a close-up view of the rigid needle in the tissue). The needle becomes soft and highly adaptable once inside biological tissue due to the effect of body temperature and can still deliver fluid while making dynamic deformations during body movement (right inset: a close-up view of the needle in a blood vessel). After use, the device remains completely soft and thus makes it non-reusable, which reduces the risk of transmission of blood-borne viruses through accidental needlestick injury among patients and healthcare providers. **e**, Photograph of commonly used IV access devices (stainless-steel needle (left) and commercial IV catheter (middle)) and the P-CARE needle (right). **f**, Performance of the IV access devices (stainless-steel needle (left) and commercial IV catheter (middle)) and the P-CARE needle (right) in soft-tissue phantom mimicking the elastic modulus of a vein (Young's modulus of 415 kPa (ref. 42); 10% oil in 33:1 PDMS). The bottom-right image highlights the softening and adapting property of the P-CARE needle after injection into the vein, which can significantly minimize the risk of tissue damage by the needle during IV administration. The dashed line outlines the softened needle in the artificial vein. Scale bars, 5 mm.

Thermal and mechanical characteristics of the P-CARE needle

The thermal and mechanical characteristics of the P-CARE needle derived from experimental and simulation studies are shown in Fig. 2. Understanding the thermal behaviour of the P-CARE needle is crucial in establishing the stiffness-varying property of the device. Figure 2a–c shows the thermal response of the P-CARE needle to temperature imitating a biological tissue environment (~37 °C). An initially rigid P-CARE needle inserted into a porcine muscle tissue model (~37 °C) becomes soft due to liquefaction of the gallium structure (Fig. 2a). The temperature transient response and associated infrared (IR) images (Fig. 2b,c) highlight the solid-to-liquid phase change of the gallium needle. The transition process of gallium is divided into
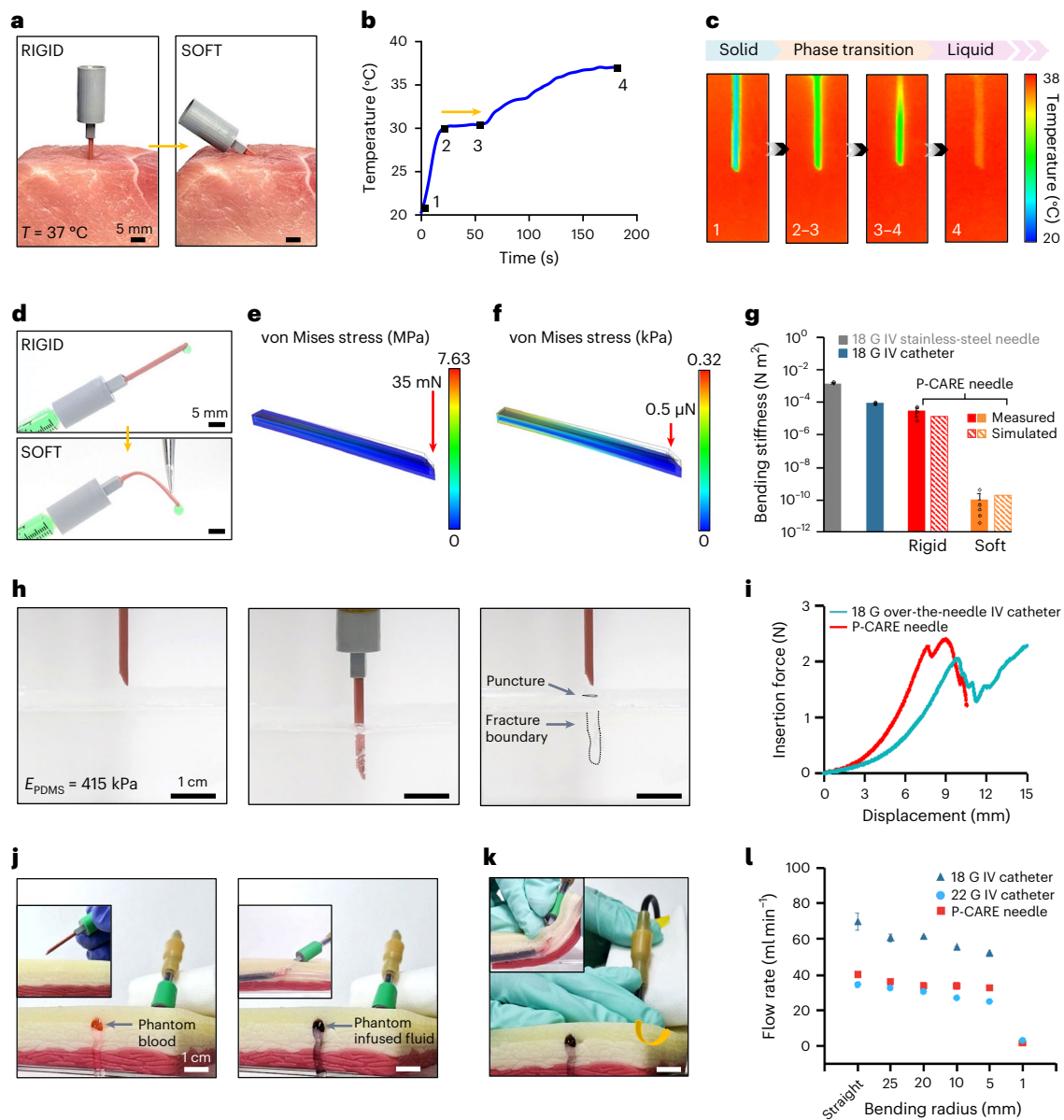
Fig. 2 | Thermal and mechanical characterization of the gallium-based P-CARE needle. a, Photographs of the P-CARE needle inserted into a porcine muscle tissue model (37 °C), showing rigid-to-soft conversion. **b**,**c**, Phase transition curve (**b**) and corresponding IR images (**c**) of the gallium needle applied with a temperature of 37 °C, showing complete solid-to-liquid transition of gallium within 60 s. Phases are indicated by numbers 1–4. **d**, Images of the P-CARE needle delivering fluid through a syringe with sample fluid. **e**,**f**, FEA simulation of the bending stiffness of the needle in the rigid (**e**) and soft (**f**) state. **g**, Plot of measured bending stiffness based on the deflection of a cantilever beam in mechanics[46]. The measured and simulated results show that the P-CARE needle in rigid mode has sufficient bending stiffness compared with an 18 G IV catheter and superior flexibility in soft mode. Data are shown as mean ± s.d. (*n* = 3 samples for stainless-steel needle and IV catheter, *n* = 4 for rigid P-CARE needle and *n* = 5 for soft P-CARE needle). **h**, Sequential images of the needle in rigid mode during

insertion and removal into/out of a phantom mimicking soft tissue (Young's modulus, *E* = 415 kPa), featuring the insertion ability of the needle (middle) which can be retrieved without buckling (right). **i**, Plot of insertion force versus depth for the P-CARE needle and standard 18 G over-the-needle IV catheter through a pig-skin, transparent-tissue phantom set-up. **j**,**k**, Operation of the P-CARE needle in tissue phantom (37 °C): in rigid mode the needle can penetrate the phantom (left; inset shows P-CARE needle in close-up); after insertion the needle becomes soft and can infuse fluid (right; inset shows infusion of fluid) (**j**); in soft mode the needle can dynamically adapt to tissue deformation, without damaging the vein, and deliver fluid (**k**). The yellow arrow in **k** depicts the bending direction of the phantom tissue model. The fluid flowing out from the hole represents blood (red) and infused fluid (violet). Scale bar, 1 cm. **l**, Flow rate as a function of bending radius for the P-CARE needle and commercial IV catheters based on a previous study[93]. Data are shown as mean ± s.d. (*n* = 3 measurements).

three distinct phases: phase 1–2 (solid phase), phase 2–3 (solid–liquid transition) and phase 3–4 (liquid phase). According to the phase transition plot measurement, it takes about 60 s for the P-CARE needle to be converted to the soft state when it is exposed to 37 °C, with negligible volume changes during phase transition. The rigid-to-soft phase transition time of the gallium-based needle could be improved by decreasing both the thickness of the gallium and the polymer encapsulant[34].

Figure 2d shows the stiffness-tuning ability of the P-CARE needle. One of the key design requirements for the variable stiffness needle is achieving sufficiently high bending stiffness in rigid mode for tissue penetration and excellent pliability in soft mode for adapting to the shape of blood vessels. The finite element analysis (FEA) simulation (Fig. 2e,f) and experimental results (Fig. 2g) show that the P-CARE needle in rigid mode has high bending stiffness (2.99×10^{-5} N m^2),

similar to that of the commercial IV catheter, ensuring soft-tissue insertion (Supplementary Figs. 3a,b). When converted to the soft mode, stiffness dramatically reduces (8.77×10^{-11} N m^2), facilitating dynamic deformation that in turn eliminates risk of mechanical damage to vessel walls[46].

To further determine the tissue-penetration ability of the rigid P-CARE needle, we formulated an artificial tissue phantom (10% oil in 33:1 PDMS) to yield the Young's modulus of a vein (~200–600 kPa (ref. [42])). Figure 2h shows the insertion of a rigid P-CARE needle into the single-block tissue phantom (modulus of 415 kPa), indicating no gross buckling of the needle during insertion and after retraction. The needle insertion demonstration in Supplementary Fig. 4a,b establishes the operating-insertion characteristics for the rigid P-CARE needle with respect to the yielded Young's modulus of artificial soft tissue based on the modulus of elasticity of a vein (~200–600 kPa (ref. [42])). Note that the elastic modulus of the vein overlaps with that of the biological tissue layers beneath the stratum corneum. This demonstration shows that the rigid needle can puncture the vein and tissue layers underneath the stratum corneum with no sign of buckling. Additional mechanical tests to characterize the mechanical property of the solid gallium-based needle under stress (Supplementary Fig. 4c,d) show that the P-CARE needle has a sufficient effective modulus (0.505 GPa at ~1% strain) for rigid insertion into soft tissues, and can sustain a compressive stress of up to 10.88 MPa (or 2.4 N applied force at the tip). On the basis of these results, the compressive strength of the rigid P-CARE needle can overcome the stress required to puncture the skin (~3.18 MPa) with an equivalent skin puncture force of 1 N (refs. [47],[48]). Furthermore, the choice of needle encapsulant for the gallium-based needle plays a vital role for a safe, rigid insertion. We intentionally bend the rigid needle using RT 623 (tear strength of 30 N mm^{-1})[49] and PDMS (2.60 N mm^{-1})[50] as encapsulant, as shown in Supplementary Fig. 4e. We observed no evidence of any sharp, pointed solid gallium (that is, an indication of mechanical damage of the needle frame) protruding out the RT 623 silicone, which shows the robustness of RT 623 as a polymeric encapsulant for rigid gallium needle frames. We conducted insertion experiments through pig skin (which is typically used for skin-related studies because of its similarity to human skin)[51] to determine the mechanical properties of the P-CARE needle during rigid insertion and compared the results with those using the standard 18 G over-the-needle IV catheter. Figure 2i shows the insertion force profile of the P-CARE needle and the standard 18 G over-the-needle IV catheter through the pig-skin, transparent-tissue phantom model. The P-CARE needle has an insertion force comparable to the standard 18 G over-the-needle IV catheter through this integrated skin-phantom set-up (see Supplementary Fig. 5a,b for insertion profile of the commercial 18 G over-the-needle IV catheter through pig skin for details). Supplementary Fig. 5c visually verifies the rigid insertion of the P-CARE needle into the pig skin. The safety and reliability of the P-CARE needle during and after rigid insertion into skin tissue can be evaluated by IR monitoring for any gallium leakage. Supplementary Fig. 5d,e shows the needle tip and the corresponding IR thermography images of the needle after tissue insertion into a porcine muscle tissue model (37 °C), indicating no signs of gallium leakage, thus verifying its safe and reliable operation.

Figure 2j,k shows the overall capability of the P-CARE needle and its potential use for IV medication using a synthetic tissue phantom with a vein hole structure that mimics biological tissue (~37 °C). In ambient conditions, the needle is stiff and can penetrate the tissue phantom, but becomes soft after insertion (Fig. 2j, left) while it delivers fluid (Fig. 2j, right). The same needle in soft mode (Fig. 2k) can dynamically adapt to tissue deformation without damaging the vein and continuously delivers fluid. In general, the softened P-CARE needle has a maximum achievable flow rate (39.92 ± 1.84 ml min^{-1}) comparable to a standard 22 G IV catheter (34.30 ± 1.59 ml min^{-1}) and is capable of reliably delivering fluid (Fig. 2l) up to a bending radius of ~5 mm (Supplementary Figs. 6 and 7). The P-CARE needle shows higher resistance to kink under

extreme bending (~1 mm) relative to the commercial 18 G IV catheter (Supplementary Fig. 8a) and comparable resistance to kink to the 22 G IV catheter. Considering the results on the maximum flow rate and previous mechanical characterization of the stiffness-tunable IV needle, the P-CARE needle has a comparable fluid-delivery performance to the standard 22 G IV catheter and a comparable mechanical property of rigid insertion to the commercial 18 G IV catheter. We simulated the condition of the softened P-CARE needle in the vein while delivering fluid (Supplementary Fig. 8b) and observed that its curvature remains unchanged by the flow rate of the fluid being delivered through the inner channel when using a typical flow rate used with standard IV catheters (that is, typical flow rate range of infused fluid is from 20 to 105 mL/min). Moreover, owing to the shortened needle length and direct connection of the needle base end to the needle hub[52], the P-CARE needle reduces the needle dead volume (19 μl) compared with the commercial IV needle (76 μl), which confirms an improved fluid-delivery efficiency (Supplementary Fig. 9). Should the proposed IV needles be used outside the hospital (for example, in mobile or portable healthcare facilities) or be transported at a warm temperature, their rigidity and shape integrity can be guaranteed by careful packaging inside a well-insulated box (made of polystyrene, for example) with reusable icepacks. The stiffness-tunable IV needle can be stored inside the polystyrene box in hot weather for more than 10 hours without becoming soft, which makes the use of the needle outdoors (35 °C) within ~30 mins possible (Extended Data Fig. 1a–c) for intended rigid insertion through the skin into vein (Extended Data Fig. 1d,e) by the attending medical professional.

Studies of in vivo biocompatibility

We evaluated the biocompatibility of the P-CARE needle by implanting sample devices (1.20 mm (h) × 1.35 mm (w) × 5 mm (l)) in the muscle of the right legs of mice[53] (Fig. 3a and Supplementary Fig. 10). For our biocompatibility test reference, we used commercially available ISO-9002-certified medical IV access devices (KoreaVaccine stainless-steel needle (18 G and 1.27 mm outer diameter)[54] and IV catheter (18 G, 1.30 mm outer diameter), which were manually cut (5 mm in length) and then inserted into the muscle of the right legs of mice. In vivo assessments of the biocompatibility of P-CARE needle samples in mice compared with those of stainless-steel needles and commercial IV catheters are summarized in Fig. 3b–g. The favourable biological impact of the RT 623–parylene N encapsulant of the proposed needle (Fig. 3b) shows the notable weight gain of mice implanted with P-CARE needle samples relative to the mice group implanted with stainless-steel needles, and a comparable body weight to the mice group with commercial IV catheter implants. Moreover, the average ratio of the weight of a major organ (the brain, lung, heart, liver, kidney and spleen, which are explanted from mice after the 14 day implantation) relative to total body weight (Fig. 3c) shows no significant differences, implying there was no significant effect on major organs after insertion of the device because of the biocompatibility of the needle encapsulant. The complete blood chemistry tests after the 14 day implantation period is shown in Fig. 3d,e. The enzyme levels related to muscle injury (that is, aspartate transaminase (AST) and lactate dehydrogenase (LDH)) are significantly reduced in the P-CARE needle group compared with the stainless-steel needle and commercial IV catheter groups, indicating less tissue (or muscle) injury induced by the P-CARE needle. These results show the superior biomechanical compatibility of the P-CARE needle compared with both stainless-steel needles and commercial IV catheters because of the ability of the softened P-CARE needle to adaptably interface with the surrounding tissues. The impact of the softening effect of the P-CARE needle can be seen in decreased levels of enzymes related to muscle and tissue injury, that is, AST and LDH (reference level for LDH, 1,590–2,610 IU L^{-1})[55], and an unchanged level of alanine aminotransferase (ALT)[56] compared with the standard IV access devices. Furthermore, enzyme levels related to normal liver (that is, ALT) and kidney (that is, blood urea nitrogen (BUN)) function,
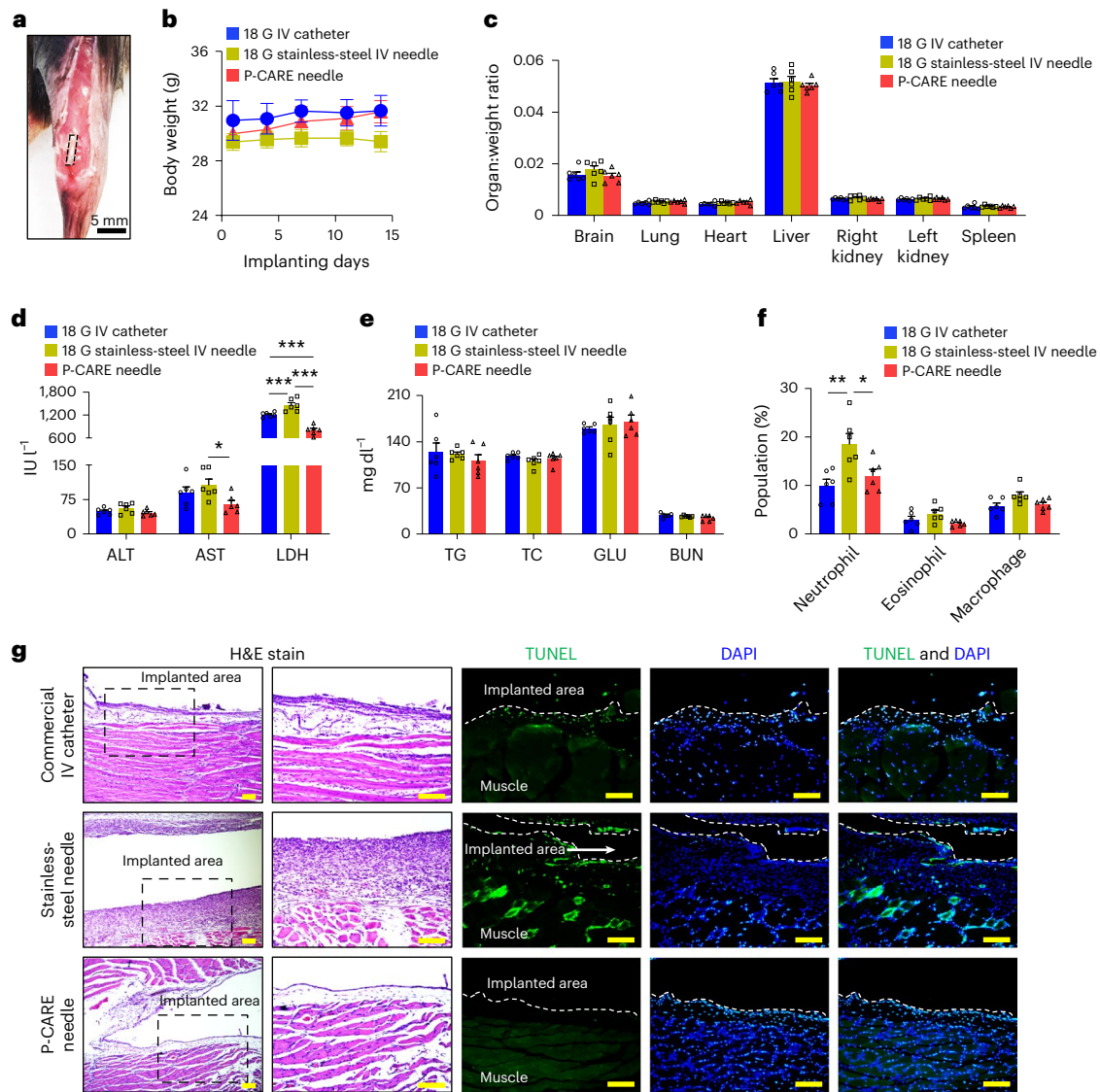
Fig. 3 | In vivo evaluations of biocompatibility of P-CARE needles in mice.
a, Image of an implanted needle sample in a leg of a mouse. The dotted line indicates the location of the implanted sample. **b**, Changes in body weight of mice in each sample group. **c**, Average organ:body weight ratio in each group after 14 days of implantation for the same groups as in **b**. Data for **b** and **c** are shown as mean ± s.e.m. (*n* = 6 mice in each group). **d**,**e**, Blood chemistry in mice for **b** and **c**: the results show that the P-CARE needle significantly decreases the enzymes related to muscle and tissue injury (AST and LDH) and has a comparable effect on liver function (ALT) (**d**) and on kidney function (BUN) and lipid metabolism (TG and TC) (**e**) compared with the commercial IV needle and catheter devices. Data are shown as mean with s.e.m. (using one-way ANOVA).

Adjusted *P* values: *P = 0.0492 for AST, ***P = 0.0001 for LDH. *n* = 6 mice in each group. **f**, Fluorescence-activated cell sorting analysis of immune cells in mice for **b** and **c**, which indicates that the P-CARE needle is capable of less muscle damage relative to the commercial stainless-steel needle and shows comparable damage to that of the commercial IV catheter. Data are shown as mean with s.e.m. (using one-way ANOVA). Adjusted *P* values for neutrophils: *P = 0.0432, **P = 0.0080. *n* = 6 mice in each group. **g**, Images of H&E stained histology (the area inside the dashed box on the left is provided in an expanded view in the right), TUNEL staining (green), DAPI staining of nuclei (blue) and co-staining (TUNEL and DAPI) of muscle tissue from **b** and **c**. Data are *n* = 6 biological replicates for each group. Scale bars, 50 μm.

and normal function of the metabolic system (that is, triglycerides (TG), total cholesterol (TC) and glucose (GLU)) for P-CARE needles and commercial IV catheters are comparable and within the reference range for C57BL/6J mice[56–58], indicating no signs of organ-specific or metabolic disorder. These results indicate that the P-CARE needle has a comparable biocompatibility to that of a commercial IV catheter because of the biocompatibility of the RT 623–Parylene N needle encapsulant. Specifically, normal quantities of ALT (16.2–85.2 IU L^{-1} (ref. 57)) and AST (52.5–268 IU L^{-1} (ref. 57)) suggest normal liver function. A normal BUN level (14.1–35.3 mg dl^{-1} (ref. 57)) indicates normal kidney function. Normal levels of TG (97.43–256.85 mg dl^{-1} (refs. 56,58)), TC (69.61–150.81 mg dl^{-1} (refs. 56,58)) and GLU (145–278 mg dl^{-1} (ref. 57)) indicate normal function of metabolic processes[59]. Further analysis

through fluorescence-activated cell sorting of immune cells (that is, neutrophils, eosinophils and macrophages) acquired from the peripheral blood of mice after the 14 day implantation period confirms the remarkable effect of the tissue-like modulus of the P-CARE needles relative to the stainless-steel needles (Fig. 3f and Supplementary Fig. 11). Neutrophil levels (that is, a marker for inflammatory change) are significantly increased in the stainless-steel needle group and similar for both the P-CARE needle and the commercial IV catheter groups, indicating that the P-CARE needle is capable of less inflammatory injury compared with the stainless-steel needle and has a damage outcome equivalent to that of the commercial IV catheter.

Images of haematoxylin-eosin (H&E) and terminal deoxynucle-otidyl transferase dUTP nick end labelling (TUNEL) stained sections of

muscle tissue surrounding the implanted site examined after the 14 day implantation period (Fig. 3g and Supplementary Fig. 12) verify the excellent pliant tissue interface of the softened P-CARE needle. H&E staining shows massive immune-cell infiltration and connective-tissue deposition around the implanted area are more severe in the stainless-steel needle group compared with the commercial IV catheter or P-CARE needle group. In the TUNEL stain of the stainless-steel group, apoptosis of several immune and muscle cells below the epithelial cell layer are identified. Considering the results of H&E and TUNEL stains, the P-CARE needle shows attenuated inflammatory change and muscle damage around the implanted area compared with the stainless-steel needle and a marginally better damage outcome compared with that of the commercial IV catheter, indicating less inflammation relative to both the stainless-steel needle and the commercial IV catheter. Overall these results indicate that the P-CARE needle has an enhanced biocompatibility compared with commercial IV access devices of comparable size. Note that the P-CARE sample devices were coated with 5-μm-thin parylene N to enhance biocompatibility and increase biofluid-barrier protection, particularly in the crevices of the inner channel[60].

In vivo assessment of fluid delivery

To evaluate the insertion and fluid-delivery performance of the P-CARE needle in vivo, we conducted an experiment on a mouse (Fig. 4). We used the laboratory mouse as our animal model as it has been greatly used as a test species in biomedical research because of their unique physiological characteristics that have a direct relation to humans in terms of thermoregulatory factors (including core temperature, lower critical ambient temperature, skin temperature and preferred ambient temperature), which are either equal to or very similar to that of the human[61]. Briefly, the mouse was anaesthetized before exposing the liver through a laparotomy followed by needle insertion into the inferior vena cava (IVC; see Methods for details). We demonstrated the ability of the P-CARE needle to puncture soft tissue and infuse fluid in vivo using an in situ closed liver perfusion in a mouse[62] (Fig. 4a). Figure 4b shows that the rigid P-CARE needle can be injected into the IVC of a mouse and deliver ethylene glycol tetraacetic acid (EGTA) solution while in its softened state. In the process, blood was easily drained from the mouse liver and the needle remained completely soft after the perfusion, indicating reliable fluid delivery after puncture and an irreversible stiffness of the needle for one-time use. The ability of the softened gallium-based needle to maintain complete softness after retraction from the IVC is accounted to a supercooling phenomenon (that is, a process in which the melted gallium remains liquid below its T_{melt} without becoming solid (Extended Data Fig. 2a,b), and is related to the characteristics of gallium)[34,63]. To further verify the fluid- or reagent-delivery function of the P-CARE needle, we evaluated the response to ethanol administration in in situ closed liver perfusion circuits. Figure 4c shows a similarly favourable fluid-delivery functionality of the P-CARE needle to that of the commercial IV catheter as the mRNA levels of the metabolic enzyme cytochrome P450 2E1 (CYP2E1) in the mouse liver tissue increase after ethanol is infused similarly to the mRNA levels in the conventional catheter group. Images of H&E- and CYP2E1-stained sections of mouse liver tissue (Fig. 4d and Supplementary Fig. 13) confirm an equivalent biocompatible fluid-delivery ability of the P-CARE needle compared with the commercial IV catheter as small lipid droplets (H&E stained) and expression of an ethanol-metabolizing enzyme (CYP2E1 stained) around the central veins increase after the infusion of ethanol similarly to the increase seen with the commercial IV catheter. These results verify the fluid-delivery capability in vivo of the P-CARE needle is comparable to that of the commercial IV catheter.

Potential on-site temperature sensing during IV infusion

As a patient receives an IV medication in a healthcare facility, changes in body temperature or an unintended leakage of infused fluid in the subcutaneous layers may occur. These conditions should be monitored as they may lead to complications[15,16,64–66]. Monitoring of core body temperature is considered to provide greater accuracy than surface body temperature[67] but it is often associated with invasive and complicated methods[68,69]. In the meantime, detection of fluid leakage during IV infusion is commonly done visually by doctors or nurses and such leakage often leads to complications (such as phlebitis) at the injection site if not detected in the early phase[70]. Although existing detection devices are reported to provide sufficient accuracy[71,72], the sensing mechanism is located over the skin surface, which is easily affected by non-steady ambient conditions. To provide better patient care during IV administration, we integrated a thin-film temperature sensor with the rigid P-CARE needle to facilitate monitoring of the core body temperature or detecting therapeutic drug leakage into subcutaneous tissue. The key characteristics of the P-CARE needle embedded with a thin-film temperature sensor are shown in Fig. 5.

Figure 5a–d and Extended Data Fig. 3a–f show the electrical characterization of the P-CARE needle with the temperature sensor. A gold thin film (180 nm thickness) with a serpentine structure sensing element is strategically located near the sharp tip of the rigid P-CARE needle to precisely capture the temperature on site (Fig. 5a). The ultrathin and flexible structure of the thin-film temperature sensor facilitates a seamless interface at strategic locations for which commercially available temperature sensors are not suitable. Figure 5b shows the relative resistance change of the sensing needle over the physiological temperature range (30–42 °C), indicating high linearity in the sensing response. We verified the electrical performance of the sensing needle during insertion and retraction into and out of a porcine tissue model (~37 °C; Fig. 5c,d). The result indicates that the needle reliably captured the temperature change during the needle insertion and retraction in soft tissue (Fig. 5d). Additional experimental results (Extended Data Fig. 3a–f) show that the temperature sensor in the P-CARE needle is independent of phase states (rigid or soft) and device encapsulation, temperature sensitive within the physiological temperature range and can withstand bending of up to a 2.5 mm radius of curvature with no significant change in sensor output. Moreover, the temperature sensing ability of the needle is independent of the flow rate at a high-flow-rate regime (240–270 ml min^{-1}), indicating the electrical output is not affected by the infusion flow rate within the range of the standard and rapid infusion flow rate of large fluid volume between 200 and 500 ml min^{-1} (ref. 73) (Supplementary Fig. 14).

Figure 5e–h and Supplementary Figs. 15 and 16 provide proof-of-concept demonstrations of the potential use of the sensing P-CARE needle to monitor on-site temperature during injection. To show the capability of the sensing needle in measuring the core body temperature, we performed an in vivo experiment in the abdomen of a mouse (Fig. 5e). The results indicate that the device can keep track of the core body temperature both before and during infusion of fluid (phosphate-buffered saline (PBS), 25 °C) peritoneally in a mouse (Fig. 5f). An additional in vivo experiment in a mouse performed peritoneally (Supplementary Fig. 15) shows that the volume of infused fluid has no significant effect on the sensor output performance, indicating the sensor is independent of the volume of the fluid injected and is only sensitive to abdominal temperature. The peritoneum is a good site for measuring the core body temperature, and this intraperitoneal (IP) temperature measurement can be considered comparable with that of veins because of tight internal body thermal regulation[68]. During IV administration in a typical hospital setting, the needle may be dislodged from the patient's vein due to the patient's movement. As a result, unintended fluid leakage into surrounding tissue layers (Fig. 5g) occurs, which is common among many patients receiving IV medication and that causes further tissue trauma at the injection site[15,16]. During this fluid leakage, there is a temperature change in the local tissue environment near the injection site[72], which suggests a potential use for the temperature-sensing needle. To show how the P-CARE needle with a temperature sensor can detect unintended fluid leakage into the
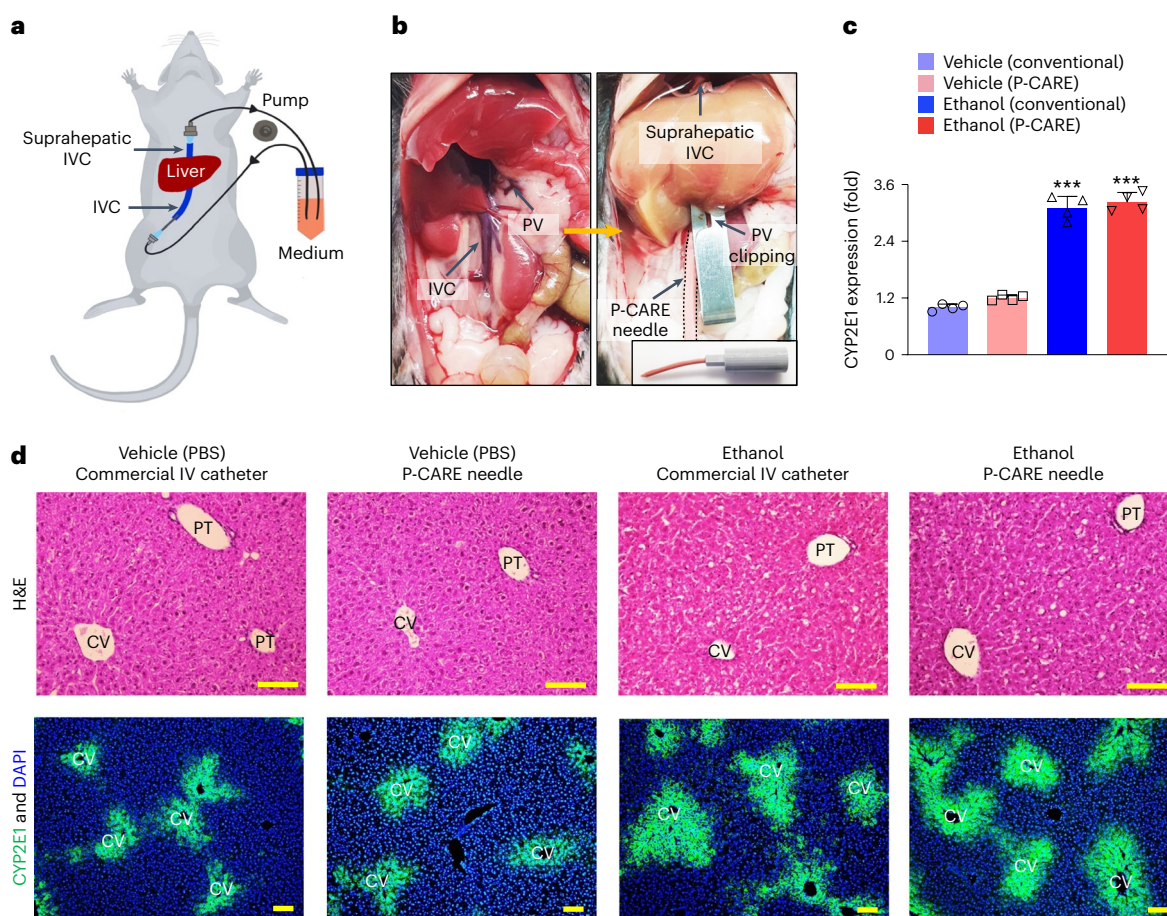
Fig. 4 | In vivo fluid-delivery effectiveness of the P-CARE needle versus the commercial IV catheter. a, Schematic of the in situ closed liver perfusion system in a mouse[62]. **b**, Images of liver perfusion in a mouse before needle insertion (left) and during perfusion through the needle (right). The P-CARE needle in the rigid state was injected into the IVC, and an EGTA solution was infused while the needle was in the soft mode, and blood could be easily drained from the liver (right; dotted lines trace the needle structure). After perfusion, the needle remained entirely soft, making it non-reusable (right, inset). **c**, Changes in CYP2E1 mRNA expression in mouse liver, showing that the P-CARE needle has a comparable fluid-delivery performance to that of the commercial IV catheter based on the increased level of the CYP2E1 metabolic enzyme. Data are shown as mean ± s.e.m.

(using one-way ANOVA). The adjusted *P* values for vehicle (conventional) and ethanol (conventional), vehicle (conventional) and ethanol (P-CARE), vehicle (P-CARE) and ethanol (conventional), and vehicle (P-CARE) and ethanol (P-CARE) are ***P < 0.0001. *n* = 4 samples for each group. Data represent *n* = 4 biological replicates for each group. **d**, Micrographs of H&E and CYP2E1 stains in a mouse liver, showing the formation of small lipid droplets (H&E) and increased CYP2E1 protein expression around the central veins (CV) after ethanol is infused, which are both associated with the biologically favourable property of the P-CARE needle compared with a commercial IV catheter. Data represent *n* = 4 biological replicates for each group. Scale bars, 50 μm. PT, portal triad; PV, portal vein.

subcutaneous tissue layer, we performed an experiment using porcine tissue (~37 °C) with an intentionally created blood vessel structure (~5 mm) to simulate an IV infusion (Supplementary Fig. 16). The porcine muscle tissue set-up was immersed in a controlled-temperature water bath (~37 °C for ~2 h) to achieve a constant temperature in the medium. The transparent tubing securely placed in the intentionally created vein structure served as a visual aid to monitor fluid delivery. We used three scenarios to clearly show the temperature sensing of the needle during drug leakage. In the first scenario, the needle was inserted into the vein structure with absolutely no infusion, which served as the controlled set-up. In the second scenario, the needle was inserted into the vein structure and fluid (25 °C) was infused. The third scenario involved modification of the second scenario, in which the needle was retracted carefully from the vein structure but remained inserted in the porcine tissue model with continuous fluid infusion (25 °C). Figure 5h shows the output of the sensing P-CARE needle from these scenarios, without infusion inside the vein (blue), during infusion inside the vein (red before 240 s), and during infusion outside the vein but within tissue (red after 240 s). The output shows that the needle can detect the occurrence of fluid leakage outside the vein structure. Collectively,

these findings show that the P-CARE needle with thermal-sensing ability can be used to monitor on-site temperature during fluid infusion, with potential use for monitoring the core body temperature or therapeutic drug leakage into subcutaneous tissue.

Discussion

The concepts, design and fabrication strategies shown here enable stiffness-tunable needles, referred to as P-CARE needles, that can potentially enhance not only the well-being of patients during prolonged therapeutic drug medication (that is, IV administration) but also the welfare of healthcare providers. The P-CARE needle is specifically designed for use inside hospital facilities (20–24 °C)[74] by medical professionals. The core base material for the needle structure is gallium, and it facilitates the stiffness and shape control of the needle based on local tissue temperature. This work shows the feasibility of the softening P-CARE needle to relieve inflammatory responses or burden in the injected site with exceptional capability of shape adapting in soft tissue compared with commercial rigid needles during prolonged IV administration (Supplementary Table 1). The excellent tissue adaptability of the softening needle during injection not only provides increased
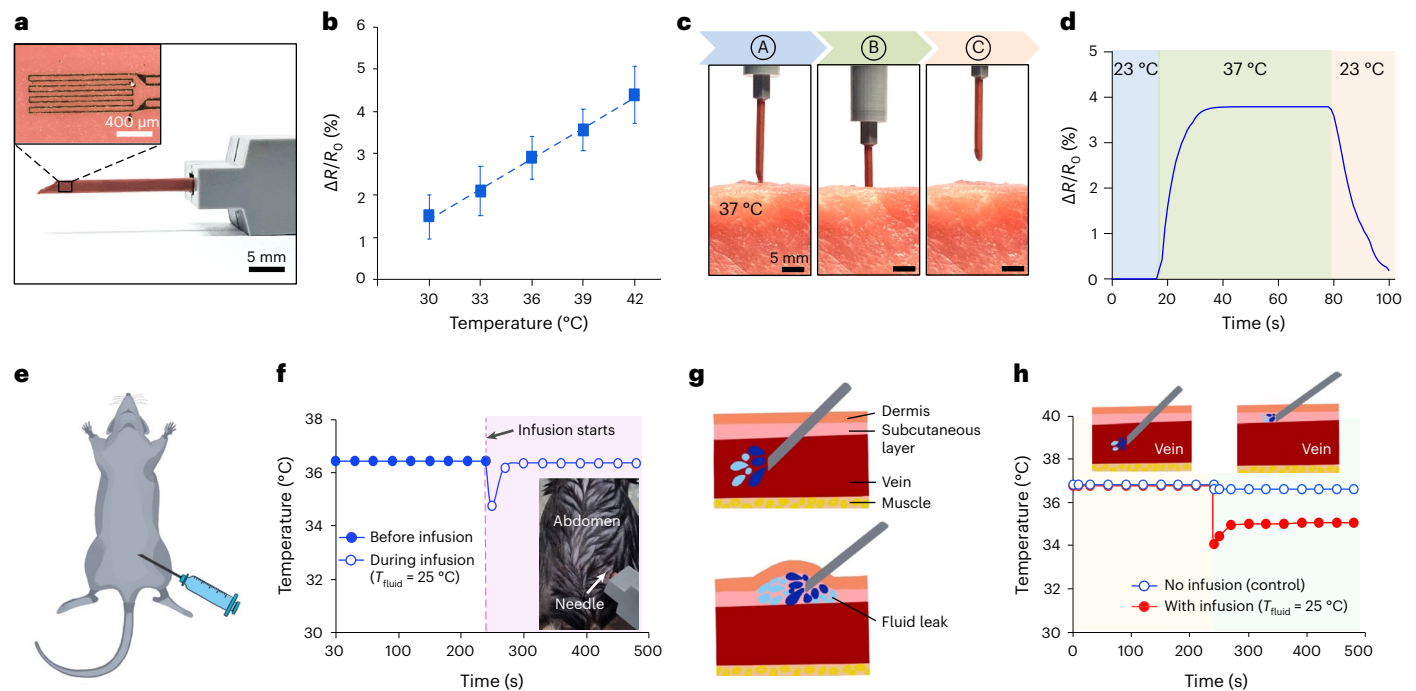
Fig. 5 | Potential utility of the P-CARE needle integrated with a temperature sensor. a, Image of a P-CARE needle integrated with a thin-film temperature sensor (inset). **b**, Relative resistance change of the temperature sensor over the physiological temperature range (30–42 °C), illustrating high linearity in sensing response. The data shows the mean ± s.d. (*n* = 3 samples, $T_{ambient}$ = 23 °C). Note: $\Delta R/R_0 = (R-R_0)/R_0$, where R_0 is the original resistance at 20 °C, and *R* is the resistance after the temperature change. **c,d**, Sequential images of needle insertion and removal in a porcine model (37 °C) (**c**), and the corresponding sensor response to the temperature change (**d**). The circled letters A, B and C correspond to the position of the needle tip with respect to the porcine muscle tissue in (**c**): before insertion (A), into the porcine muscle tissue (B), and after insertion (C). For (**d**): $\Delta R/R_0 = (R-R_0)/R_0$, where R_0 is the original resistance at

20 °C, and *R* is the resistance after the temperature change. **e,f**, Illustration of IP access of the sensor-integrated needle (**e**) as a way to measure the core body temperature, and the corresponding sensor response before and during infusion in vivo (**f**). The result shows the device can monitor the core body temperature both before (filled points) and during (open points) infusion. The equivalent temperature was obtained based on the sensor calibration shown in **b**. **g,h**, Illustration of normal IV infusion (top) and fluid leak into the subcutaneous layer due to needle movement out of the vein (bottom) (**g**), and device detection of fluid leak outside the vein structure during simulated IV infusion in a porcine tissue model (**h**) (Supplementary Fig. 16). The experiment verifies the capability of the P-CARE needle to detect fluid leak into the subcutaneous layer.

mobility among hospitalized patients receiving continuous IV medication but also alleviates the discomfort arising from the required replacement or re-siting of rigid indwelling IV catheters every 3–4 days, which is thought to reduce the risk of bloodstream infections (such as nosocomial bacteraemia) and phlebitis[17]. The P-CARE needle with its enhanced biocompatibility is a promising tool to re-evaluate the necessity for routine catheter replacement as inflammation injury in the indwelling site can be significantly reduced compared with commercial IV catheters based on our 14 day experimental animal study. We showed that the needle has sufficient stiffness for tissue insertion followed by fluid delivery and vein targeting using ex vivo porcine tissue and porcine skin models, an alternative experimental model set-up in line with ISO 10993-1:2018 (an international standard, used to evaluate and test medical devices, that recognizes other alternative experimental set-ups 'to minimize the number and exposure of test animals')[75]. By integrating a thin-film temperature sensor with the needle, the real-time monitoring of temperature on site during IV medication is possible, which would allow for monitoring of body temperature or of undesirable fluid leakage into subcutaneous layers, without the need for additional medical tools and procedures.

Compared with previous studies on soft and adaptable devices that require mechanical support for rigid insertion (such as an insertion shuttle)[45,76] that offer limited stiffness control (soft or flexible only)[77,78], have a slow-to-moderate tissue-adaptability response time[45,76–79] or that have limited functionality (either probe insertion, fluid delivery or direct tissue-interfacing only)[76–78], the P-CARE needle has several unique merits (Supplementary Table 2). The gallium-based

needle is capable of stand-alone, tunable stiffness control via a body temperature stimulus (a stiffness-tuning ratio that is two orders of magnitude higher than that of shape-memory polymers)[79], facilitating a sufficiently high modulus in the rigid state for rigid insertion into soft tissues and an exceptional low modulus in the soft state for a compliant tissue interface within ~1 min. The multifunctional and single-use assembly of the P-CARE needle allows for several functions in one device (rigid tissue insertion, fluid delivery, temperature sensing and an adaptive tissue interface, all in one unit) that can improve use and handling operation with minimal complexities. Furthermore, the irreversible softness of the P-CARE needle (because of the supercooling phenomenon) after one use is a promising strategy for safe handling, disposal, and to prevent needlestick injuries and needle reuse[34,63].

For medical applications requiring longer needles (as in cancer diagnosis[80] and haemodialysis[81]), new phase-change materials may need to be investigated to further increase the stiffness in the rigid mode and enhance the stiffness variability. In addition, the modulus of elasticity of the softened P-CARE needle can be further tuned to match other organs with a different Young's modulus by using other soft encapsulants (such as Ecoflex (0.07 MPa)[82] or PDMS (1 MPa)[50]) to more closely match the Young's modulus of the target organs (such as the spleen, 0.02–0.652 MPa (ref. [83]); the gall bladder, 0.23–0.67 MPa (ref. [84]); the liver, 0.27–0.39 MPa (ref. [85]); the kidney, 0.18 MPa (ref. [86]); the urinary bladder, 0.25 MPa (ref. [87]); or the colon, 0.9 MPa (ref. [88])). Another method for tuning the modulus of elasticity is through the modification of the base:curing agent component mixing ratio of a specific encapsulant polymer (Supplementary Table 3).

In summary, we have described the fundamentals for designing a stiffness-tunable smart needle and sharp medical tools that offer enhanced biomechanical compatibility and after-use safety-handling features. The devices may be applied in many other settings of clinical significance. Also, they may offer solutions for the worldwide call by the WHO towards the prevention of reusing needles and unsafe injection practices[31].

Methods

This study complies with all relevant ethical regulations. All animal protocols were approved by the Institutional Animal Care and Use Committee of Korea Advanced Institute of Science and Technology (KAIST; KA2021-71).

Fabrication of the P-CARE needle with a thin-film temperature sensor

The fabrication of the needle began with three-dimensional (3D) printing (Core 530; B9Creations) of reusable moulds for the gallium needle frame and polymer encapsulation using pre-determined patterns and a stereolithographic process using a UV-sensitive resin (B9R-8-HD Slate; B9Creations). The reusable moulds for gallium needle frame and polymer encapsulation were cured in room-temperature condition (~10 hour, 23 °C) to ensure complete curing of the micro-thin patterns. The rectangular needle frame structure was developed by first fabricating a PDMS (Sylgard 184; Dow Corning) mould cast on the 3D-printed mould. After complete curing of PDMS (~70 °C for 30 min), the PDMS layer was delaminated from the 3D-printed mould and securely clipped onto a glass slide (75 mm × 50 mm × 1 mm). Approximately 0.5 ml of liquid gallium (Ga metal 99.99; RotoMetals) was extracted from its container through a disposable needle syringe (Kovax Syringe) then injected into the PDMS mould–glass interface. After solidifying the gallium in a freezer (~10 °C for 15 min), the gallium-based needle frame was carefully retrieved from the mould. The fluidic channel and encapsulation were fabricated through drop casting of elastomer (Elastosil RT 623; Wacker) onto the 3D-printed mould for encapsulation. The cured inner polymeric channel was interfaced in between the two U-channel gallium-based frames, whereas the cured outer encapsulation enveloped the outer area of the entire needle structure. A drop of uncured Ecoflex (00-30; Smooth-On), manually spread between the gallium and RT 623 needle frame interface, forms a thin layer of adhesion. Subsequently, the polymeric needle is attached into a customized 3D-printed needle hub, with the needle base having direct contact with the hub. An appropriate amount of epoxy resin (5 Minute Epoxy; Permatex) ensures a reliable and robust integration at the needle base–hub interface. The fluid delivery of the needle was manually tested by pushing de-ionized water through a commercial 1 ml syringe (Kovax Syringe) plugged into the needle hub (4 mm inner diameter). Details on the fabrication of each needle component can be found in Supplementary Fig. 1.

Fabrication and integration of a thin-film temperature with the P-CARE needle

A separately fabricated thin-film temperature sensor was manually stacked onto one of the outer surfaces of the polymeric needle under an optical microscope (OM4713; Omano). The temperature sensor was fabricated with Cr/Au (10 nm/180 nm) serpentine traces on a 3.6-μm-thick polyethylene terephthalate (Chemplex Industries) through photolithography. An anisotropic conductive film was bonded to the electrodes of the sensor to interface with the external electronic circuit through electrical interconnectors (Cr/Au, 10 nm/180 nm) developed by photolithography. Subsequently, a thin layer of cured RT 623 was carefully laminated on top of the sensor with a thin layer of uncured Ecoflex 00-30 (Fig. 1a,b). Finally, the completed device was coated with 7-μm-thick parylene N (K1 Solution) to protect the metal electrodes from biofluid for in vivo experiments.

Bending stiffness measurement

Bending stiffness, or flexural rigidity, of a needle or catheter was determined using the deflection of a cantilever beam in mechanics[46] by obtaining the deflection according to the concentrated force. For deflection measurements[34], the needle or catheter base end is fixed while the other end is loaded with a concentrated force. For conventional IV access devices, deflection due to the concentrated force was obtained using a force gauge (Series 5 M5-05; Mark-10). For the P-CARE needle, the deflection due to its own weight and concentrated force was determined using an optical camera and force gauge (Series 5 M5-05; Mark-10) at two distinct temperatures (23 °C and 37 °C) for characterization of the device in rigid and soft mode. Subsequently, bending stiffness (EI) was calculated using the equation EI = $(FL^3)/3\delta$ where F, δ and L represent concentrated force, deflection and length of the beam, respectively.

Mechanical modelling and FEA

FEA simulation of the P-CARE needle for bending. A structural analysis for simulating the bending stiffness of the P-CARE needle in rigid and soft mode was conducted through FEA (COMSOL Multiphysics v.5.3a; COMSOL). The polymeric needle was modelled as a linear elastic material model (for the gallium-based needle frame, Young's modulus of 9.8 GPa and 30 kPa at rigid and soft mode, respectively, Poisson ratio of 0.475 and density of 5,910 kg m^{-3} (ref. 35); and for RT 623 encapsulation, Young's modulus of 290 kPa (ref. 89), Poisson ratio of 0.49 and density of 1,140 kg m^{-3}). Fixed constraint was applied at the needle base end while a concentrated downward force was applied at the needle tip. The applied forces at the needle tip in rigid and soft mode were 35 mN and 0.5 μN, respectively. The bending stiffness (EI) for rigid and soft mode was calculated based on the simulated deflection values using the equation EI = $(FL^3)/3\delta$ where F, δ and L represent concentrated force, deflection and length of the needle, respectively (Fig. 2e,f).

Modelling simulation of needle–tissue interaction. Three-dimensional modelling and simulation of the needle–tissue interaction during needle insertion was performed to verify if the needle can puncture the soft vein tissue (COMSOL Multiphysics v.5.3a; COMSOL). Stationary solid mechanics was used to model the stresses in the tissue (Young's modulus of 600 kPa (ref. 42), Poisson's ratio of 0.49 (ref. 90) and density of 1,080 kg m^{-3} (ref. 90)) by constructing a simple rectangular box. The polymeric needle was assumed to be a linear elastic material (Young's modulus of 9.8 GPa, Poisson's ratio of 0.475 and density of 5,910 kg m^{-3}). An insertion force of 1 N was applied at the needle base end[91] with an angle of insertion of 25°, following typical IV injection procedure in a hospital setting. All surfaces of the tissue model, except the top surface, used fix constraints, assuming that the force exerted by the needle onto the tissue would have no significant effect on the nearby tissue surrounding the insertion region. The resulting mechanical stress experienced by the tissue was then obtained from the generated von Mises stress to determine if the needle punctured the soft vein tissue (that is, stress needed to puncture the tissue is at ~3 MPa (ref. 47); Supplementary Fig. 3).

Needle insertion profiling

For testing needle insertion through skin, an integrated porcine skin, multilayer PDMS and oil tissue phantom was used (Fig. 2i and Supplementary Fig. 5a–c). The porcine skin was purchased from a local butcher shop and used within 2 hours after purchase. Thus, ethical approval was not required.

Experiments on animal subjects

C57BL/6J male mice (27–30 g, 12 weeks old) were purchased from a specific-pathogen-free facility (KAIST) and maintained on a regular 12 hour light–12 hour dark cycle. The mice were transferred to a room in the laboratory and they remained in the same room for at least 1

week before the in vivo experiments for biocompatibility and fluid- or reagent-delivery tests to minimize stress from transport. No statistical methods were used to pre-determine sample sizes but our sample sizes are similar to those reported in previous publications[34,92]. In all in vivo experiments, including the biocompatibility and fluid-delivery tests, C57BL/6J male mice with similar dates of birth were randomly allocated to each experimental group. For core body temperature sensing by the device during infusion in mice, mice were randomly selected among the group of mice in one cage and animals were excluded in cases where the temperature gradient was not established at the injection site during infusion. The exclusion criteria were pre-established. Data collection and analysis were not performed blind to the conditions of the experiments.

Biocompatibility test

For the surgical procedure to implant the device for the biocompatibility test (Supplementary Fig. 10), each mouse received anaesthesia through IP injection of a mixture of ketamine and xylazine (C57BL/6J male mice, 27–30 g, 12 weeks old, 6 mice for each group). After shaving the hair in the implanting area of the right leg of the mouse, the skin was sterilized with 70% ethanol. A 1 cm skin incision was made in the thigh, followed by dissection of the right thigh muscle. Each sample device (that is, stainless steel (18 G), commercial IV catheter (18 G) and P-CARE needle (1.20 mm × 1.35 mm)), manually cut to a length of 5 mm, was implanted in the dissected muscle, and the muscle layer and the skin layer were sequentially sutured using 4-0 black silk (Ailee). The body weight of each mouse was measured twice a week during the 14 day biocompatibility test period. Mice were killed after the 14 day device implantation period for blood chemistry, histological and flow cytometry analysis.

Serum biochemical measurement

Mouse (C57BL/6J male mice, 27–30 g, 12 weeks old, 6 mice for each group) serum was collected from the peripheral blood and the levels of LDH, AST, ALT, TG, TC and BUN were analysed using VetTest Chemistry Analyzer (IDEXX Laboratories) according to the manufacturer's instructions. Blood GLU level was measured with a glucometer (Allmedicus).

Flow cytometry analysis

Immune cells (that is, neutrophils, eosinophils and macrophages) were extracted from the peripheral blood of mice and subjected to flow cytometry analysis (C57BL/6J male mice, 27–30 g, 12 weeks old, 6 mice for each group). The isolated cells were first incubated with the LIVE/DEAD Fixable Aqua Dead Cell Stain Kit for 405 nm excitation (Thermo Fisher Scientific) to identify live or dead cells. Cells were then labelled with fluorescence-tagged antibodies using anti-mouse eFluor 450-conjugated CD45 (catalogue number 48-0451-82; Thermo Fisher Scientific), FITC-conjugated F4/80 (catalogue number 11-4801-02; eBioscience), PerCP-Cy5.5-conjugated Ly-6G (catalogue number 560602; BD Biosciences), PE-CF594-conjugated Siglec-F (catalogue number 562757; BD Biosciences) and APC-Cy7-conjugated CD11b (catalogue number 561039; BD Biosciences) under the anti-mouse CD16/CD32 (mouse Fc blocker, catalogue number 553142; BD Biosciences). Stained cells were read with the LSRFortessa X-20 (BD Bioscience). Neutrophils (CD11b$^+$Ly6G$^+$), eosinophils (CD11b$^+$Siglec-F$^+$) and macrophages (F4/80$^+$CD11b$^+$) were analysed with FlowJo software (v.10.81; FlowJo) using pseudo-colour analysis plots.

Liver perfusion test in a mouse

In situ closed liver perfusion in a mouse was performed as previously described[62]. Briefly, the mouse was anaesthetized through IP injection with a mixture of ketamine and xylazine in PBS to expose the liver through laparotomy (diluted ketamine:xylazine:PBS ratio of 5:2:7). The infrahepatic IVC was cannulated with a 22 G angiocatheter (catalogue number 4030; Jelco) and the portal vein was cut. Pre-warmed

PBS was infused for 5 minutes to extract the blood in the liver. Once the blood in the liver was extracted, which can be confirmed through liver discolouration, the chest was opened to expose the right atrium of the heart. Then, using another angiocatheter, the suprahepatic IVC was cannulated by puncturing the right atrium of the heart. A 1 ml syringe was connected to the suprahepatic IVC catheter to work as a reservoir. After the closed circuit was established, an experimental medium (that is, low-GLU DMEM with 10% fetal bovine serum and 1% penicillin–streptomycin; Welgene) was circulated for 2 hours. Ethanol and vehicle (PBS) were used for the experimental condition. Note that the successful cannulation of the P-CARE needle (Fig. 4b) was first verified on a separate experiment by infusing EGTA solution through the IVC to extract the blood in the liver while the portal vein was cut. A complete liver blood extraction can be confirmed through liver discolouration.

Histological analysis

Histological analysis was performed for the muscle tissue from the right thigh of mice extracted after the 14 day period of the biocompatibility test, and liver tissue (that is, left and medial lobes) extracted after the 2 hour in situ closed circulation (C57BL/6J male mice, 27–30 g, 12 weeks old, 6 mice for each group). Muscle and liver tissues were fixed overnight with 10% neutral buffered formalin (catalogue number F5554; Sigma-Aldrich). Paraffin-embedded tissues were thinly sectioned (that is, 4 µm thickness) and stained by H&E reagent followed by immunostaining. After de-paraffinization and rehydration, the tissue was transferred to a 10 mM citrate buffer followed by antigen retrieval using a microwave for 5 minutes. For TUNEL staining, the data protocol of the In Situ Cell Death Detection Kit, Fluorescein (catalogue number 11684795910; Roche) was followed. For immunofluorescence staining of CYP2E1 in liver tissue, primary antibodies (1:200 diluted in PBS, catalogue number AB1252; Millipore) and secondary antibodies (1:300 diluted in PBS, catalogue number ab150073; Abcam) were incubated overnight at 4 °C and 1 hour at room temperature, respectively. Finally, DAPI solution (catalogue number ab104139; Abcam) was used as mounting medium for the tissue samples for nucleus detection. Histological images were captured using an Olympus BX51 microscope equipped with a CCD camera (Olympus) and imaging analysis was conducted with DP2-BSW.

Quantitative real-time PCR

Total RNA was isolated from liver tissue or cells (C57BL/6J male mice, 27–30 g, 12 weeks old) using TriZol reagent (catalogue number 15596-018; Thermo Fisher Scientific) according to the manufacturer's instructions. The same quantity of total RNA was reverse transcribed to complementary DNA using ReverTra Ace qPCR RT Master Mix with gDNA Remover (catalogue number 611500; Toyobo). Quantitative real-time PCR (qRT-PCR) was performed using SYBR Green Real-Time PCR Master Mix (catalogue number 128200; Toyobo). To quantify transcription, the result was normalized with 18S. The primer sequences for 18S and *Cyp2e1* for qRT-PCR are as follows: 18S forward, ACAGGATTGACAGATTGATAGC, and 18S reverse, GCCAGAGTCTCGTTCGTTA; and *Cyp2e1* forward, CCAC-CCTCCTCCTCGTAT, and *Cyp2e1* reverse, CTTGACAGCCTTGTAGCC.

Temperature sensing of needle with integrated thin-film temperature sensor

To show the potential use of the P-CARE needle integrated with a thin-film sensor for in-body temperature sensing, an in vivo experiment was performed in a mouse (C57BL/6J male mouse, 27–30 g, 12 weeks old) through IP access (Fig. 5e). The preparation of the mouse for the experiment began with an injection of anaesthesia with a mixture of ketamine and xylazine to the back of the neck of the mouse before it was transferred on the surgery table. To prohibit any movement of the mouse during the experiment, the hands and feet of the mouse were fastened to the surgery table using board pins. The abdominal region

of the mouse was then cleansed with 70% ethanol. The rigid P-CARE needle integrated with a thin-film temperature sensor was carefully inserted into the right side of the peritoneal cavity through a small incision (~1 mm) of the skin layer of the mouse. Resistance measurement was performed using a four-point probe-resistance technique with a constant current of 1 mA (Supplementary Fig. 2). The relative resistance change of the device was then monitored both before and during fluid infusion, with a 30 second recording interval. The fluid (PBS), which was kept at a temperature of ~25 °C (Digital Precise Water Bath WB-6; Daihan Scientific), was infused at a flow rate of 0.5 ml min^{-1} (205S fluid pump; Watson Marlow). Subsequently, the equivalent temperature was obtained using the sensor calibration plot curve (shown in Fig. 5b) of the resistance–temperature relationship (Fig. 5f). To show the potential utility of the needle integrated with the thin-film sensor to detect unwanted fluid leakage during IV infusion, an ex vivo experiment was performed using porcine muscle tissue (Supplementary Fig. 16), which was purchased from a local butcher shop and used within 2 hours after purchase. Thus, ethical approval was not required.

Data presentation and statistical analysis
All values are given as individual data points and are shown as mean ± s.e.m. or mean with s.d., unless otherwise noted. Animal data were analysed for statistical significance by one-way analysis of variance (ANOVA) with Tukey's multiple comparisons correction, as implemented in GraphPad Prism 8.

Reporting summary
Further information on research design is available in the Nature Portfolio Reporting Summary linked to this article.

Data availability
The main data supporting the results in this study are available within the paper and its Supplementary Information. The raw and analysed datasets generated during the study are available for research purposes from the corresponding authors on reasonable request. Source data for the figures are provided with this paper.

References

1. Boras, B. et al. Preclinical characterization of an intravenous coronavirus 3CL protease inhibitor for the potential treatment of COVID19. *Nat. Commun.* **12**, 6055 (2021).
2. Ma, F. et al. Neurotransmitter-derived lipidoids (NT-lipidoids) for enhanced brain delivery through intravenous injection. *Sci. Adv.* **6**, eabb4429 (2020).
3. FDA approves first treatment for COVID-19. *US Food and Drug Administration* https://www.fda.gov/news-events/press-announcements/fda-approves-first-treatment-covid-19 (2020).
4. Wei, F., Chen, W. & Lin, X. A clinical rule for the difficulty prediction on scalp intravenous access in infants (SIAI) from emergency room. *Sci. Rep.* **10**, 6624 (2020).
5. Finfer, S., Myburgh, J. & Bellomo, R. Intravenous fluid therapy in critically ill adults. *Nat. Rev. Nephrol.* **14**, 541–557 (2018).
6. Samson, A. et al. Intravenous delivery of oncolytic reovirus to brain tumor patients immunologically primes for subsequent checkpoint blockade. *Sci. Transl. Med.* **10**, eaam7577 (2018).
7. Zingg, W. & Pittet, D. Peripheral venous catheters: an under-evaluated problem. *Int. J. Antimicrob. Agents* **34**, S38–S42 (2009).
8. Rickard, C. M., McCann, D., Munnings, J. & McGrail, M. R. Routine resite of peripheral intravenous devices every 3 days did not reduce complications compared with clinically indicated resite: a randomised controlled trial. *BMC Med.* **8**, 53 (2010).
9. Jin, J. et al. The optimal choice of medication administration route regarding intravenous, intramuscular, and subcutaneous injection. *Patient Prefer. Adherence* **9**, 923–942 (2015).
10. Malach, T. et al. Prospective surveillance of phlebitis associated with peripheral intravenous catheters. *Am. J. Infect. Control* **34**, 308–312 (2006).
11. Duffy, B. L. & Lee, J. S. Intravenous access: a comparison of two methods. *Anaesth. Intensive Care* **11**, 135–137 (1983).
12. Weiss, D., Yaakobovitch, H., Tal, S., Nyska, A. & Rotman, O. M. Novel short peripheral catheter design for prevention of thrombophlebitis. *J. Thromb. Haemost.* **17**, 39–51 (2019).
13. Abolfotouh, M. A., Salam, M., Bani-Mustafa, A., White, D. & Balkhy, H. H. Prospective study of incidence and predictors of peripheral intravenous catheter-induced complications. *Ther. Clin. Risk Manag.* **10**, 993–1001 (2014).
14. Miliani, K. et al. Peripheral venous catheter-related adverse events: evaluation from a multicentre epidemiological study in France (the CATHEVAL Project). *PLoS ONE* **12**, e0168637 (2017).
15. Kim, J. T., Park, J. Y., Lee, H. J. & Cheon, Y. J. Guidelines for the management of extravasation. *J. Educ. Eval. Health Prof.* **17**, 21 (2020).
16. Al-Benna, S., O'Boyle, C. & Holley, J. Extravasation injuries in adults. *ISRN Dermatol.* **2013**, 856541 (2013).
17. Webster, J., Osborne, S., Rickard, C. M. & Marsh, N. Clinically-indicated replacement versus routine replacement of peripheral venous catheters. *Cochrane Database Syst. Rev.* **2019**, CD007798 (2019).
18. Alexandrou, E. et al. International prevalence of the use of peripheral intravenous catheters. *J. Hosp. Med.* **10**, 530–533 (2015).
19. Wallis, M. C. et al. Risk factors for peripheral intravenous catheter failure: a multivariate analysis of data from a randomized controlled trial. *Infect. Control Hosp. Epidemiol.* **35**, 63–68 (2014).
20. Weber, P. W. et al. Modifying peripheral IV catheters with side holes and side slits results in favorable changes in fluid dynamic properties during the injection of iodinated contrast material. *AJR Am. J. Roentgenol.* **193**, 970–977 (2009).
21. Xu, Y. et al. Hydrogel-coated needles prevent puncture site bleeding in arteriovenous fistula and arteriovenous grafts in rats. *Biomed. Pharmacother.* **143**, 112113 (2021).
22. Yu, H. et al. Water-insoluble polymeric guanidine derivative and application in the preparation of antibacterial coating of catheter. *ACS Appl. Mater. Interfaces* **10**, 39257–39267 (2018).
23. Travessa, D., Ferrante, M. & den Ouden, G. Diffusion bonding of aluminium oxide to stainless steel using stress relief interlayers. *Mater. Sci. Eng. A* **337**, 287–296 (2002).
24. Phua, S. L. et al. Reinforcement of polyether polyurethane with dopamine-modified clay: the role of interfacial hydrogen bonding. *ACS Appl. Mater. Interfaces* **4**, 4571–4578 (2012).
25. Ebnesajjad, S. in *Fluoroplastics* 2nd edn, Vol. 2 (ed Ebnesajjad, S.) 216–235 https://doi.org/10.1016/B978-1-4557-3197-8.00009-2 (William Andrew Publishing, 2015).
26. Li, C., Guan, G., Reif, R., Huang, Z. & Wang, R. K. Determining elastic properties of skin by measuring surface waves from an impulse mechanical stimulus using phase-sensitive optical coherence tomography. *J. R. Soc. Interface* **9**, 831–841 (2012).
27. Alfulayw, K. H., Al-Otaibi, S. T. & Alqahtani, H. A. Factors associated with needlestick injuries among healthcare workers: implications for prevention. *BMC Health Serv. Res.* **21**, 1074 (2021).
28. Beltrami, E. M., Williams, I. T., Shapiro, C. N. & Chamberland, M. E. Risk and management of blood-borne infections in health care workers. *Clin. Microbiol. Rev.* **13**, 385–407 (2000).
29. Khan Afridi, A. A., Kumar, A. & Sayani, R. Needle stick injuries—risk and preventive factors: a study among health care workers in tertiary care hospitals in Pakistan. *Glob. J. Health Sci.* **5**, 85–92 (2013).
30. Schuurmans, J., Lutgens, S. P., Groen, L. & Schneeberger, P. M. Do safety engineered devices reduce needlestick injuries? *J. Hosp. Infect.* **100**, 99–104 (2018).

31. *WHO Guideline on the Use of Safety-Engineered Syringes for Intramuscular, Intradermal and Subcutaneous Injections in Health Care Settings* (World Health Organization, 2016).

32. Harb, A. C. et al. Safety engineered injection devices for intramuscular, subcutaneous and intradermal injections in healthcare delivery settings: a systematic review and meta-analysis. *BMC Nurs.* **14**, 71 (2015).

33. Byun, S.-H., Sim, J. Y., Agno, K.-C. & Jeong, J.-W. Materials and manufacturing strategies for mechanically transformative electronics. *Mater. Today Adv.* **7**, 100089 (2020).

34. Byun, S.-H. et al. Mechanically transformative electronics, sensors, and implantable devices. *Sci. Adv.* **5**, eaay0418 (2019).

35. Lin, Y., Genzer, J. & Dickey, M. D. Attributes, fabrication, and applications of gallium-based liquid metal particles. *Adv. Sci.* **7**, 2000192 (2020).

36. Elbourne, A. et al. Antibacterial liquid metals: biofilm treatment via magnetic activation. *ACS Nano* **14**, 802–817 (2020).

37. Lu, Y. et al. Transformable liquid-metal nanomedicine. *Nat. Commun.* **6**, 10066 (2015).

38. Chen, M. et al. Self-powered multifunctional sensing based on super-elastic fibers by soluble-core thermal drawing. *Nat. Commun.* **12**, 1416 (2021).

39. Yan, W. et al. Thermally drawn advanced functional fibers: new frontier of flexible electronics. *Mater. Today* **35**, 168–194 (2020).

40. Qu, Y. et al. Superelastic multimaterial electronic and photonic fibers and devices via thermal drawing. *Adv. Mater.* **30**, 1707251 (2018).

41. Wen, X. et al. Flexible, multifunctional neural probe with liquid metal enabled, ultra-large tunable stiffness for deep-brain chemical sensing and agent delivery. *Biosens. Bioelectron.* **131**, 37–45 (2019).

42. Ebrahimi, A. P. Mechanical properties of normal and diseased cerebrovascular system. *J. Vasc. Interv. Neurol.* **2**, 155–162 (2009).

43. Bai, M.-Y., Chang, Y.-C. & Chu, J. P. Preclinical studies of non-stick thin film metallic glass-coated syringe needles. *Sci. Rep.* **10**, 20313 (2020).

44. Hauzenberger, J. R. et al. Systematic in vivo evaluation of the time-dependent inflammatory response to steel and Teflon insulin infusion catheters. *Sci. Rep.* **8**, 1132 (2018).

45. Jeong, J.-W. et al. Wireless optofluidic systems for programmable in vivo pharmacology and optogenetics. *Cell* **162**, 662–674 (2015).

46. I. Mechanical properties of catheters. *Acta Radiol. Diagn.* **4**, 11–22 https://doi.org/10.1080/05678066609170493 (1966).

47. Makvandi, P. et al. Engineering microneedle patches for improved penetration: analysis, skin models and factors affecting needle insertion. *Nanomicro. Lett.* **13**, 93 (2021).

48. Kataoka, H. et al. Measurement of the tip and friction force acting on a needle during penetration. In *Proc. 5th Medical Image Computing and Computer-Assisted Intervention (MICCAI 2002)* (eds Dohi, T. & Kikinis, R.) 216–223 (Springer, 2002).

49. Elastosil RT 623 A/B datasheet version 1.3 (Wacker Chemie, 2014).

50. Sylgard 184 silicone elastomer datasheet reference number 10-1204A-01 (Dow Corning, 1998).

51. Summerfield, A., Meurens, F. & Ricklin, M. E. The immunology of the porcine skin and its value as a model for human skin. *Mol. Immunol.* **66**, 14–21 (2015).

52. Chitnis, G. D. et al. A resistance-sensing mechanical injector for the precise delivery of liquids to target tissue. *Nat. Biomed. Eng.* **3**, 621–631 (2019).

53. Yu, Y. et al. Biocompatibility and in vivo operation of implantable mesoporous PVDF-based nanogenerators. *Nano Energy* **27**, 275–281 (2016).

54. KoreaVaccine catalogue (KoreaVaccine, 2016).

55. Nathwani, R. A., Pais, S., Reynolds, T. B. & Kaplowitz, N. Serum alanine aminotransferase in skeletal muscle diseases. *Hepatology* **41**, 380–382 (2005).

56. Mazzaccara, C. et al. Age-related reference intervals of the main biochemical and hematological parameters in C57BL/6J, 129SV/EV and C3H/HeJ mouse strains. *PLoS ONE* **3**, e3772 (2008).

57. Harrison, S. D. Jr, Burdeshaw, J. A., Crosby, R. G., Cusic, A. M. & Denine, E. P. Hematology and clinical chemistry reference values for C57BL/6 X DBA/2 F1 mice. *Cancer Res.* **38**, 2636–2639 (1978).

58. Haney, E. M. et al. in *Screening for Lipid Disorders in Children and Adolescents* (Agency for Healthcare Research and Quality (US), 2007).

59. Guo, H. et al. Advanced materials in wireless, implantable electrical stimulators that offer rapid rates of bioresorption for peripheral axon regeneration. *Adv. Funct. Mater.* **31**, 2102724 (2021).

60. Kim, B. J. & Meng, E. Micromachining of parylene C for bioMEMS. *Polym. Adv. Technol.* **27**, 564–576 (2016).

61. Gordon, C. J. The mouse thermoregulatory system: its impact on translating biomedical data to humans. *Physiol. Behav.* **179**, 55–66 (2017).

62. Choi, W.-M. et al. Experimental applications of in situ liver perfusion machinery for the study of liver disease. *Mol. Cells* **42**, 45–55 (2019).

63. Li, X. F. et al. Size–temperature phase diagram of gallium. *EPL* **94**, 16001 (2011).

64. Fink, E. L., Kochanek, P. M., Clark, R. S. B. & Bell, M. J. Fever control and application of hypothermia using intravenous cold saline. *Pediatr. Crit. Care Med.* **13**, 80–84 (2012).

65. Obořilová, A., Mayer, J., Pospíšil, Z. & Kořistek, Z. Symptomatic intravenous antipyretic therapy: efficacy of metamizol, diclofenac, and propacetamol. *J. Pain Symptom Manage.* **24**, 608–615 (2002).

66. Schell-Chaple, H. M., Liu, K. D., Matthay, M. A., Sessler, D. I. & Puntillo, K. A. Effects of IV acetaminophen on core body temperature and hemodynamic responses in febrile critically ill adults: a randomized controlled trial. *Crit. Care Med.* **45**, 1199–1207 (2017).

67. Richmond, V. L., Davey, S., Griggs, K. & Havenith, G. Prediction of core body temperature from multiple variables. *Ann. Occup. Hyg.* **59**, 1168–1178 (2015).

68. Sessler, D. I., Warner, D. S. & Warner, M. A. Temperature monitoring and perioperative thermoregulation. *Anesthesiology* **109**, 318–338 (2008).

69. Moons, C. P., Hermans, K., Remie, R., Duchateau, L. & Odberg, F. Intraperitoneal versus subcutaneous telemetry devices in young Mongolian gerbils (*Meriones unguiculatus*). *Lab. Anim.* **41**, 262–269 (2007).

70. Lim, R., Damalerio, R. B., Bong, C. L., Tan, S. K. & Cheng, M.-Y. Novel conformal skin patch with embedded thin-film electrodes for early detection of extravasation. *Sensors* **21**, 3429 (2021).

71. Bicen, A. O., West, L. L., Cesar, L. & Inan, O. T. Toward non-invasive and automatic intravenous infiltration detection: evaluation of bioimpedance and skin strain in a pig model. *IEEE J. Transl. Eng. Health Med.* **6**, 4100207 (2018).

72. Shekalim, A. Method and device for detecting extravasation. US patent 6,425,878 B1 (2002).

73. Ross, P. A., Lerman, J. & Coté, C. J. in *A Practice of Anesthesia for Infants and Children* 6th edn (eds Coté, C. J. et al.) 1175–1203.e8 https://doi.org/10.1016/B978-0-323-42974-0.00052-5 (Elsevier, 2019).

74. *ANSI/ASHRAE/ASHE Addendum A to ANSI/ASHRAE/ASHE Standard 170-2017 Ventilation of Healthcare Facilities* (ASHRAE, 2020).

75. *ISO 10993-1:2018 Biological Evaluation of Medical Devices—Part 1: Evaluation and Testing within a Risk Management Process* (International Organization for Standardization, 2018).

76. Samant, P. P. & Prausnitz, M. R. Mechanisms of sampling interstitial fluid from skin using a microneedle patch. *Proc. Natl Acad. Sci. USA* **115**, 4583–4588 (2018).

77. Liu, Y. et al. Morphing electronics enable neuromodulation in growing tissue. *Nat. Biotechnol.* **38**, 1031–1036 (2020).

78. Sunwoo, S. H. et al. Chronic and acute stress monitoring by electrophysiological signals from adrenal gland. *Proc. Natl Acad. Sci. USA* **116**, 1146–1151 (2019).

79. Reeder, J. et al. Mechanically adaptive organic transistors for implantable electronics. *Adv. Mater.* **26**, 4967–4973 (2014).

80. Gupta, S. & Madoff, D. C. Image-guided percutaneous needle biopsy in cancer diagnosis and staging. *Tech. Vasc. Interv. Radiol.* **10**, 88–101 (2007).

81. Marticorena, R. M. & Donnelly, S. M. Impact of needles in vascular access for hemodialysis. *J. Vasc. Access* **17**, S32–S37 (2016).

82. Series safety data sheet SDS no. 823A (Smooth-On, 2023); https://www.smooth-on.com/msds/files/BD_DS_Eco_Equ_EZB_EZS_Psy_MS_OOMOO_Reb_ST_SS_Soma_Sol_Sorta.pdf

83. Stingl, J. et al. Morphology and some biomechanical properties of human liver and spleen. *Surg. Radiol. Anat.* **24**, 285–289 (2002).

84. Karimi, A., Shojaei, A. & Tehrani, P. Measurement of the mechanical properties of the human gallbladder. *J. Med. Eng. Technol.* **41**, 541–545 (2017).

85. Mattei, G. & Ahluwalia, A. Sample, testing and analysis variables affecting liver mechanical properties: a review. *Acta Biomater.* **45**, 60–71 (2016).

86. Karimi, A. & Shojaei, A. Measurement of the mechanical properties of the human kidney. *IRBM* **38**, 292–297 (2017).

87. Dahms, Piechota, Dahiya, Lue & Tanagho Composition and biomechanical properties of the bladder acellular matrix graft: comparative analysis in rat, pig and human. *Br. J. Urol.* **82**, 411–419 (1998).

88. Egorov, V. I., Schastlivtsev, I. V., Prut, E. V., Baranov, A. O. & Turusov, R. A. Mechanical properties of the human gastrointestinal tract. *J. Biomech.* **35**, 1417–1425 (2002).

89. Byun, S.-H. et al. Design strategy for transformative electronic system toward rapid, bidirectional stiffness tuning using graphene and flexible thermoelectric device interfaces. *Adv. Mater.* **33**, 2007239 (2021).

90. Li, C., Huang, Z. & Wang, R. K. Elastic properties of soft tissue-mimicking phantoms assessed by combined use of laser ultrasonics and low coherence interferometry. *Opt. Express* **19**, 10153–10163 (2011).

91. Kobayashi, Y. et al. Use of puncture force measurement to investigate the conditions of blood vessel needle insertion. *Med. Eng. Phys.* **35**, 684–689 (2013).

92. Kalidasan, V. et al. Wirelessly operated bioelectronic sutures for the monitoring of deep surgical wounds. *Nat. Biomed. Eng.* **5**, 1217–1227 (2021).

93. Nagle, R., Schreiber, K. & Said, T. An evaluation of the effect of a kinked cannula on intravenous cannula flow rates. *Bahrain Med. Bull.* **37**, 175–177 (2015).

Author contributions

K.-C.A. and J.-W.J. conceptualized the project and designed the experiments for overall technology development. K.-C.A., S.-H.B., S.O., S.L., H.K. and S.C. fabricated and prepared the devices, discussed conceptual illustration, and captured the photographs for proof-of-concept demonstration and set-up. K.Y., K.K. and W.-I.J. designed and performed the experiments, collected data and analysed results in the in vivo biocompatibility and fluid-delivery tests. K.-C.A. and K.Y. performed the in vivo temperature sensing under the supervision of W.-I.J. and J.-W.J. K.-C.A., K.Y., W.-I.J. and J.-W.J. performed the investigation, analysed the data and wrote the results. K.-C.A. and J.-W.J. were responsible for conceptual drawings and data representation. K.-C.A., K.Y., W.-I.J. and J.-W.J. wrote the article. W.-I.J. and J.-W.J. acquired funding and supervised the project. W.-I.J. and J.-W.J. are co-senior authors. All authors discussed the results and contributed to revision of the article.

Competing interests

The authors declare no competing interests.

Additional information

Extended data is available for this paper at https://doi.org/10.1038/s41551-023-01116-z.

Supplementary information The online version contains supplementary material available at https://doi.org/10.1038/s41551-023-01116-z.

Correspondence and requests for materials should be addressed to Won-Il Jeong or Jae-Woong Jeong.

Peer review information *Nature Biomedical Engineering* thanks Giuseppe Barillaro, Eoin O'Cearbhaill and the other, anonymous, reviewer(s) for their contribution to the peer review of this work.
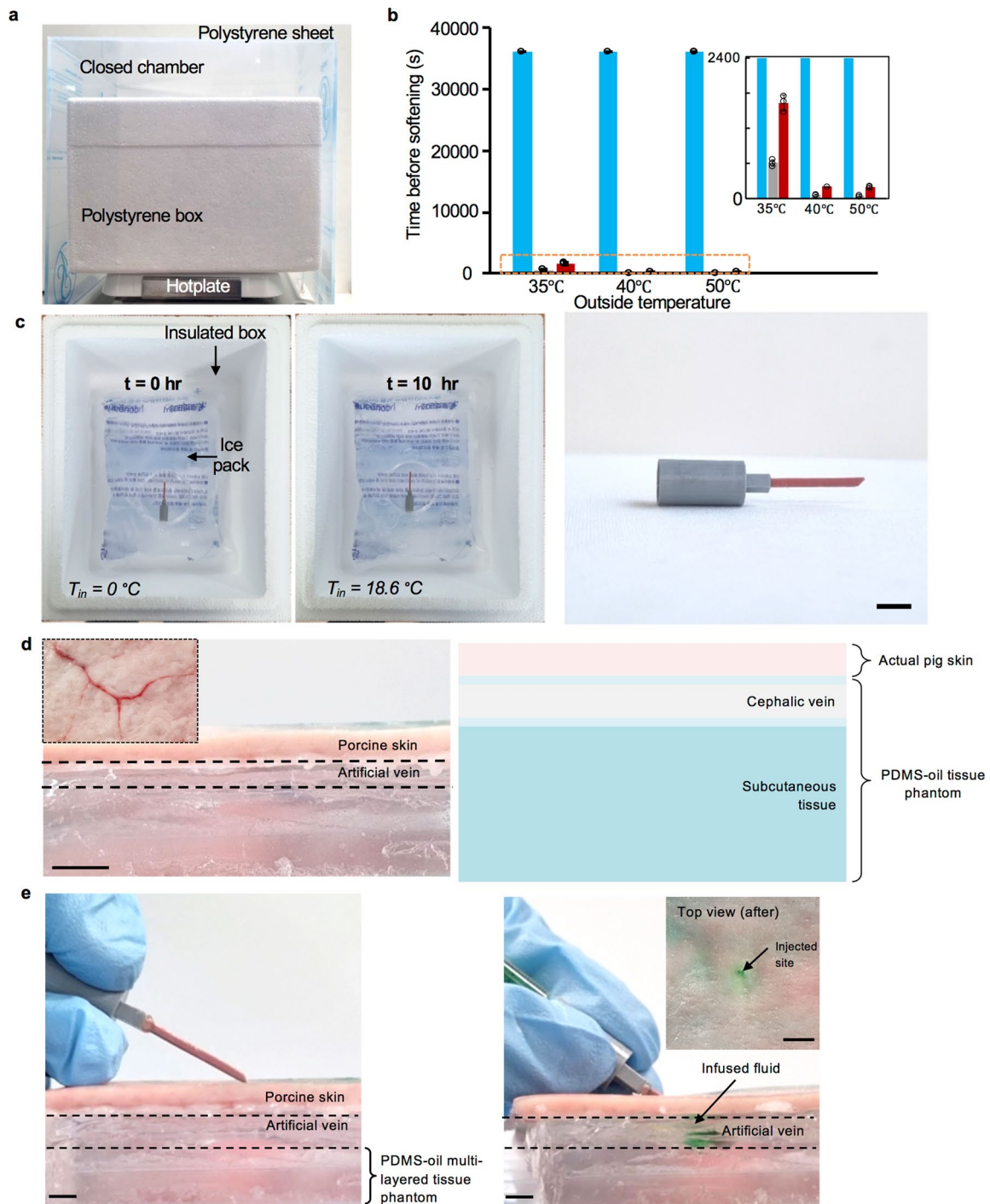
Reprints and permissions information is available at www.nature.com/reprints.

**Extended Data Fig. 1 | Stiffness- and shape-integrity of P-CARE needle under warm temperature. a**, Image of the temperature-controlled experimental set-up in cross section view. **b**, Plot of time before the needle becomes soft at various temperatures. The plot legends are as follows: blue, the needle is inside the polystyrene box with icepacks; grey, the needle is taken out from the polystyrene box without icepacks; red, the needle is taken out from the polystyrene box with icepacks. The inset shows the magnified plots for the softening time at indicated outside temperatures. Data are presented as mean values ± SD (n = 3 samples). **c**, Images showing the physical condition of the needle inside the polystyrene box with icepacks, externally heated to 50 °C, (left) needle inside the polystyrene box before heating, (middle) needle inside the polystyrene after 10 hrs of heating on a hotplate (50 °C) in a closed chamber, (right) needle taken out from the insulated

box with icepack after 10 hrs of heating at 50 °C. Scale bar, 1 cm. **d**, Images of the integrated pig skin-transparent multi-layer tissue phantom with artificial vein setup, (left) side view image of the skin-multi-layer transparent tissue phantom, (left, inset) actual image of porcine skin showing small superficial veins in an upside-down view, ~1.5 mm thickness, (right) schematic illustration of integrated pig skin-transparent multi-layer tissue phantom created by using PDMS-oil (10:1 by weight), 13 mm total thickness. Scale bar, 1 cm. **e**, Images of the rigid insertion of the needle into porcine skin followed by fluid delivery into a customized vein-transparent tissue phantom with an external temperature of 35 °C, highlighting that a rigid insertion through pig skin using P-CARE needle is possible. Scale bars, 5 mm.

a

b
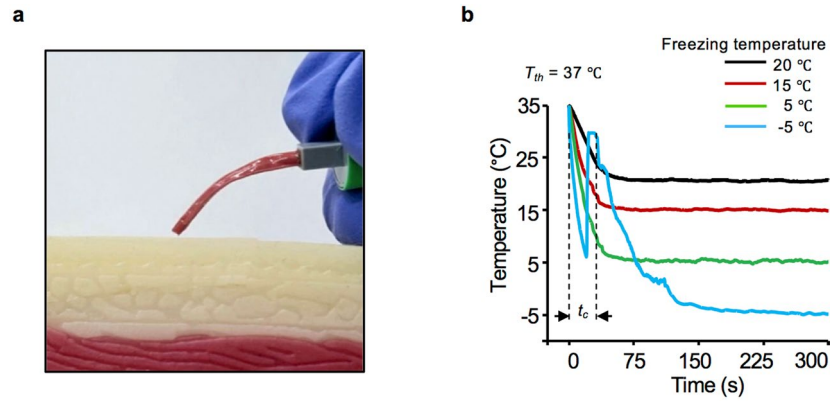
Extended Data Fig. 2 | P-CARE needle after insertion and fluid delivery.
a, Image after retracting the softened P-CARE needle from tissue phantom, demonstrating a gravity-bent and completely softened needle after use for an advance safe-handling needle disposal. **b**, Plot of thermal response during the freezing process of the softened P-CARE needle after usage (that is, rigid insertion). The solidification of the softened needle occurs when the needle

was exposed to temperature of −5 °C. At this temperature, it takes about 29.45 s for the gallium needle to solidify (tc), verifying that the softened needle after use (that is, withdrawn from the soft tissue after rigid insertion) will indefinitely exhibit a low modulus of elasticity when use at a healthcare facility (20–24 °C), making the needle completely non-reusable after first usage.
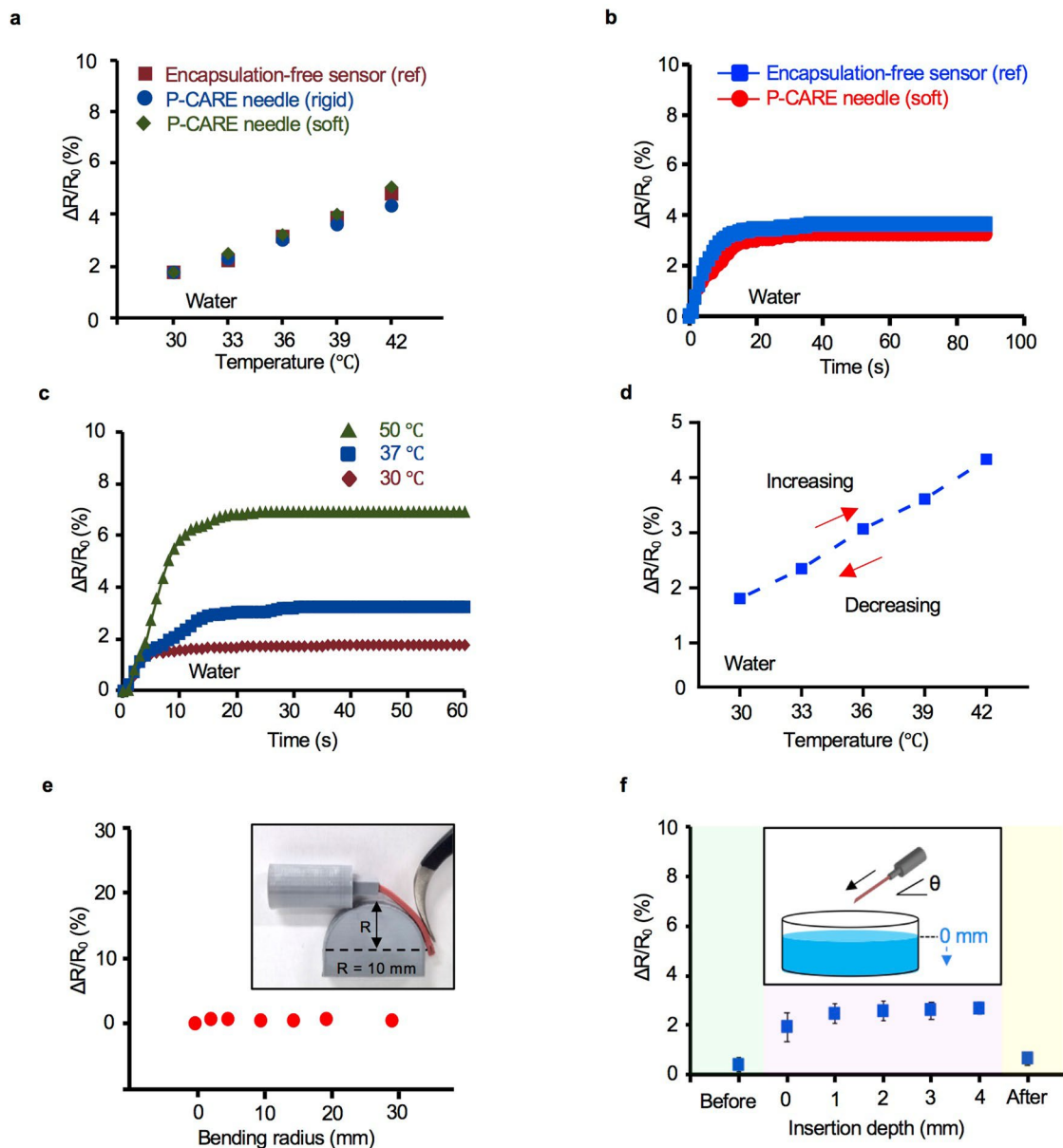
Extended Data Fig. 3 | Characterization of nanomembrane temperature sensor integrated in P-CARE needle. a, Relative resistance change as a function of temperature, showing that the phase state of P-CARE needle (rigid or soft) has no significant effect on the sensing performance (Tambient= 20 °C) within physiological temperature range (30 to 42 °C). Note that the same sample was measured repeatedly (n = 3 trials). **b**, Relative resistance change as a function of time, exhibiting that the encapsulated P-CARE needle sensor has a comparable thermal response time (~9 s) with the one of an encapsulation-free thin-film sensor of the same design when immersed in the same medium (Tmedium= 37 °C, Tambient= 25 °C). The slight difference between sensor output is attributed to the polymeric encapsulation of the device. **c**, Relative resistance change as a function of time of P-CARE needle immersed in a medium of varying temperature

(30, 37 and 50 °C). **d**, Relative resistance change as a function of increasing or decreasing medium temperature, demonstrating no significant device hysteresis within physiological temperature range. Note that the same sample was measured repeatedly (n = 3 trials). **e**, Plot of sensor output as a function of radius of curvature, indicating electrical stability during bending. **f**, Relative resistance change as a function of insertion depth into a medium with constant temperature. The result exhibits that the sensor output is independent of insertion depth as needle advances deeper (75% of total needle length is immersed, which is similar to the conventional practice in IV needle placement in a healthcare setting) into a temperature-controlled environment (Tmedium = 36 °C; Tambient = 24 °C; θ = ~30°). Error bars show the mean ± standard deviation (n = 3 samples).

nature portfolio

Corresponding author(s): Won-Il Jeong and Jae-Woong Jeong

Last updated by author(s): Feb 21, 2023

Reporting Summary

Nature Portfolio wishes to improve the reproducibility of the work that we publish. This form provides structure for consistency and transparency in reporting. For further information on Nature Portfolio policies, see our Editorial Policies and the Editorial Policy Checklist.

Statistics

For all statistical analyses, confirm that the following items are present in the figure legend, table legend, main text, or Methods section.

n/a	Confirmed	
☐	☒	The exact sample size (n) for each experimental group/condition, given as a discrete number and unit of measurement
☐	☒	A statement on whether measurements were taken from distinct samples or whether the same sample was measured repeatedly
☐	☒	The statistical test(s) used AND whether they are one- or two-sided *Only common tests should be described solely by name; describe more complex techniques in the Methods section.*
☒	☐	A description of all covariates tested
☒	☐	A description of any assumptions or corrections, such as tests of normality and adjustment for multiple comparisons
☐	☒	A full description of the statistical parameters including central tendency (e.g. means) or other basic estimates (e.g. regression coefficient) AND variation (e.g. standard deviation) or associated estimates of uncertainty (e.g. confidence intervals)
☐	☒	For null hypothesis testing, the test statistic (e.g. F, t, r) with confidence intervals, effect sizes, degrees of freedom and P value noted *Give P values as exact values whenever suitable.*
☒	☐	For Bayesian analysis, information on the choice of priors and Markov chain Monte Carlo settings
☒	☐	For hierarchical and complex designs, identification of the appropriate level for tests and full reporting of outcomes
☒	☐	Estimates of effect sizes (e.g. Cohen's d, Pearson's r), indicating how they were calculated

Our web collection on statistics for biologists contains articles on many of the points above.

Software and code

Policy information about availability of computer code

Data collection	No software was used for data collection.
Data analysis	For flow-cytometry analysis: Stained cells were read with LSRFortessa X-20 (BD Bioscience). Neutrophils (CD11b+Ly6G+), eosinophils (CD11b+SiglecF+), and macrophages (F4/80+CD11b+) were analysed with FlowJo software (version 10.81; FlowJo LLC, BD bioscience) through a pseudo-color analysis plot.

For manuscripts utilizing custom algorithms or software that are central to the research but not yet described in published literature, software must be made available to editors and reviewers. We strongly encourage code deposition in a community repository (e.g. GitHub). See the Nature Portfolio guidelines for submitting code & software for further information.

Data

Policy information about availability of data

All manuscripts must include a data availability statement. This statement should provide the following information, where applicable:
- Accession codes, unique identifiers, or web links for publicly available datasets
- A description of any restrictions on data availability
- For clinical datasets or third party data, please ensure that the statement adheres to our policy

The main data supporting the results in this study are available within the paper and its Supplementary Information. Source data for the figures are provided with this paper. The raw and analysed datasets generated during the study are available for research purposes from the corresponding authors on reasonable request.

Field-specific reporting

Please select the one below that is the best fit for your research. If you are not sure, read the appropriate sections before making your selection.

☒ Life sciences   ☐ Behavioural & social sciences   ☐ Ecological, evolutionary & environmental sciences

For a reference copy of the document with all sections, see nature.com/documents/nr-reporting-summary-flat.pdf

Life sciences study design

All studies must disclose on these points even when the disclosure is negative.

Sample size	For the in vivo biocompatibility studies, the sample size of the mice group was selected by referring to the biocompatibility tests described in Nat. Biomed. Eng 5, 1217–1227 (2021); doi:10.1038/s41551-021-00802-0, and in Sci. Adv. 5, eaay0418 (2019); doi: 10.1126/sciadv.aay0418.
Data exclusions	For core-body-temperature sensing with the device during infusion in mice, the animals were excluded in cases where a temperature gradient was not established at the injected site during infusion. The exclusion criteria were pre-established.
Replication	In each independent in vivo experiments, all experimental findings showed reproducible results in duplicates. And all attempts at replication were successful.
Randomization	In all in vivo experiments including biocompatibility tests and fluid-delivery tests, C57BL/6J males mice with similar date of birth were randomly allocated to each experimental group. For core-body-temperature sensing with the device during infusion in mice, the mice were randomly selected among the mice group from one cage.
Blinding	Considering our experimental design, blinding was impossible because we analysed the mouse phenotype after device implantation on the initial day.

Reporting for specific materials, systems and methods

We require information from authors about some types of materials, experimental systems and methods used in many studies. Here, indicate whether each material, system or method listed is relevant to your study. If you are not sure if a list item applies to your research, read the appropriate section before selecting a response.

Materials & experimental systems

n/a	Involved in the study
☒	☐ Antibodies
☒	☐ Eukaryotic cell lines
☒	☐ Palaeontology and archaeology
☐	☒ Animals and other organisms
☒	☐ Human research participants
☒	☐ Clinical data
☒	☐ Dual use research of concern

Methods

n/a	Involved in the study
☒	☐ ChIP-seq
☐	☒ Flow cytometry
☒	☐ MRI-based neuroimaging

Animals and other organisms

Policy information about studies involving animals; ARRIVE guidelines recommended for reporting animal research

Laboratory animals	C57BL/6J male mice, 12-weeks old. The mice were managed on a regular light–dark cycle (12-h light – 12-h dark) in a specific pathogen-free facility in KAIST. The temperature and humidity of the facility were maintained at 24 °C and 40–60 %.
Wild animals	The study did not involve wild animals.
Field-collected samples	The study did not involve samples collected from the filed.
Ethics oversight	All animal protocols were approved by the Institutional Animal Care and Use Committee of Korea Advanced Institute of Science and Technology (KAIST), Daejeon, South Korea (KA2021-71). The porcine tissue and porcine skin used for the ex vivo experiments were purchased from a local butcher shop. No approval was needed.

Note that full information on the approval of the study protocol must also be provided in the manuscript.

Flow Cytometry

Plots

Confirm that:

☒ The axis labels state the marker and fluorochrome used (e.g. CD4-FITC).

☒ The axis scales are clearly visible. Include numbers along axes only for bottom left plot of group (a 'group' is an analysis of identical markers).

☒ All plots are contour plots with outliers or pseudocolor plots.

☒ A numerical value for number of cells or percentage (with statistics) is provided.

Methodology

Sample preparation	Immune cells (neutrophils, eosinophils and macrophages) were extracted from the peripheral blood of mice and subjected to flow-cytometry analysis.
Instrument	LSRFortessa X-20 (BD Bioscience)
Software	FlowJo (version 10.81; FlowJo LLC)
Cell population abundance	Detailed cell-population abundance is described in the relevant figures.
Gating strategy	Neutrophils (CD11b+Ly6G+), eosinophils (CD11b+SiglecF+), and macrophages (F4/80+CD11b+) were analysed .

☒ Tick this box to confirm that a figure exemplifying the gating strategy is provided in the Supplementary Information.